THE MICROFLUIDIC COMPONENTS OF THE FREEFORM STIMULATOR FOR NEURAL MODULATION

by
Chaojun Cheng

A dissertation submitted to Johns Hopkins University in conformity with the requirements for

the degree of Doctor of Philosophy

Baltimore, Maryland
August 2022

Abstract

Electronic devices can be interfaced with tissue via metal electrodes to deliver electrical current to stimulate target neurons for disease treatment. Different from the charge-balanced short pulse that can be safely applied in biology, direct current (DC) has been restricted from being applied for prolonged durations due to the toxicity generated by electrolysis around stimulation electrodes. On the other hand, as revealed by acute studies in animals, DC can be applied to suppress neural activity, a potential beneficial function for vestibular implants and devices intended to block pain signal in peripheral nerves or to treat epilepsy. To enable the use of prolonged DC in a human body, we developed a novel device we named Freeform Stimulator (FS). It is designed to safely deliver DC to neurons for arbitrary long durations without causing electrolysis. FS uses two pairs of electrodes to deliver charge-balanced currents into a microfluidic (μF) channel network. The induced ionic currents in the μF can be rectified into an ionic DC at the output of the device by the cyclical operation of two embedded valves that control the conduction of the channel network.

ABSTRACT

FS could provide a way to safely apply prolonged DC in human body and benefit those applications that use DC to modulate neural activity. This thesis is focused on the development of the µF components that are required in the µF chip of FS which includes a shape memory alloy valve used to control ionic current, an ionic transistor that can be used as a non-mechanical control of ionic current and an ionic current sensor used to measure the ionic DC output. For proof of concept of FS, we tested the obtained µF chip with properly designed control of current and valve and succeeded in rectifying the ionic currents in µF into an ionic DC at the output.

Primary Reader and Advisor: Gene Y. Fridman

Secondary Readers: Charles C. Della Santina, Sean Sun

Contents

CONTENTS

CONTENTS

List of Figures

LIST OF FIGURES

LIST OF FIGURES

Chapter 1

Introduction

Neurons use ions as charge carriers to regulate some important cell functions such as firing of action potential and muscle contraction. [1] In neural engineering, electronic devices can be interfaced with the human body to apply ionic current via metal electrodes to modulate cell activities for treatment of neural disorders. [2] For example, a pacemaker can be implanted in a patient's chest to help control the heartbeat by stimulating heart muscle with electrical pulses [3]; a cochlear implant can electrically stimulate the cochlear nerve to restore hearing function [4]; a vestibular implant can be used to electrically stimulate the vestibular nerve to restore vestibular sensation [5]. However, delivering direct current (DC) via electrode can cause irreversible electrochemical reaction which generates toxicity and damage neurons. [6] To address this safety constraint, the delivered current has been restricted to be charge-balanced biphasic pulses to eliminate the undesired toxicity generation in neural implants. [7] By limiting the amount of injected

charge of the first pulse below a threshold known as the electrode's charge injection capacity (CIC), [8] the conversion of electronic/ionic currents at the electrode is restricted to reversible processes such as accumulation of charges at the electrode/electrolyte interface and reversible electrochemical reactions. Subsequently, an opposite pulse with equivalent amount of extraction of charge reverses the electrochemical process caused by the first pulse such that the net charge injection at the electrode becomes zero and the electrode can safely deliver pulses without causing electrolysis. [9]

On the other hand, in laboratory research, DC has been shown effective in inhibiting neural activities which could be promising for treating some neural disorders. [10]–[16] In a study of epilepsy treatment, applying cathodic DC in the epileptogenic regions of a rat brain showed a noticeable reduction of pathological brain activity. [17] In another study of peripheral nerve pain block, applying DC to the sciatic nerve was effective in blocking the A-delta fibers, which propagate pain signals. [18] Another example of effective DC suppression is in the vestibular system. The vestibular system of the inner ear provides the sensation of head rotation and linear acceleration. DC was shown effective in being able to not only increase, but also decrease the firing rate of the vestibular nerve relative to its spontaneous activity. This bidirectional regulation was shown to restore a wider range of head velocity sensation compared to using pulse frequency modulation (PFM) which is the standard technique used in conventional implantable pulse generators (IPG). [19]

CHAPTER 1

To enable the use of DC in neural modulation, we developed a device called freeform stimulator (FS) that is intended to apply DC safely without the concern of irreversible electrochemical reactions. [20] Figure 1.1 diagrams the working principle of the FS. The FS delivers charge-balanced pulses into the microfluidic (µF) via four electrodes (E1, E1', E2 and E2'). [21] The electronic current supplied to the electrodes by the current source will be converted into the equivalent ionic current carried by the ions in the electrolyte via the electrode/electrolyte interface. The two valves (v1 and v2) are operated to open/close the channels cyclically such that the ionic current passing within the µF can be rectified into an ionic DC at its output connected with tissue. [22] The FS can be seen as an ionic version of AC to DC bridge rectifier [23] which uses actively controlled valves
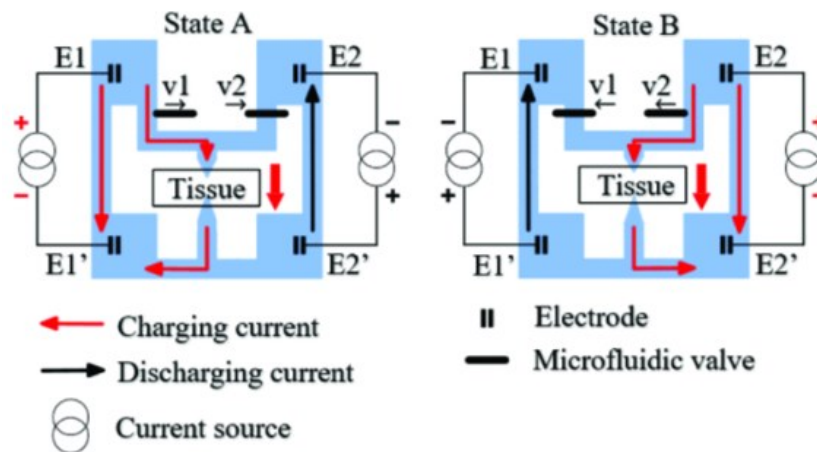
Figure 1.1 The schematic of freeform stimulator with two operational states.
E1 (E1') and E2 (E2') electrodes are controlled to deliver charge-balanced currents into the microfluidic channel network filled with saline (blue). The red/black arrows are charging/discharging ionic current passing through the channels. States A and B are two cyclically repeating states of the same freeform stimulator. To rectify the injected ionic currents into an ionic direct current (DC) through the tissue, valves 1 (v1) and 2 (v2) open and close accordingly with the direction of the current applied by the two independent current sources.

to rectify the ionic current within a µF chip instead of diodes that rectify the current in the electronic analog. This two-valve design is improved from its original four-valve design in which the discharging channels are controlled by two additional valves. [22] The two-valve design outperforms the four-valve design in terms of operational reliability and power consumption due to the reduced number of the actuators. However, the current efficiency of the FS (the ratio of the therapeutic current delivered to tissue over the current delivered by the embedded electrodes) with this two-valve design is less than one as the charging current (red arrows) can pass through the uncontrolled discharging channel. The current efficiency can be increased by increasing the impedance of the discharging channels which adversely increases the required compliance voltage during the discharging phase (black arrows). The choice of the impedance of the discharging channel is a result of a trade-off between the current efficiency and the required compliance voltage.

FS provides a way to apply prolonged DC to tissue without the concern of the toxicity generated by electrolysis and could directly benefit those applications that apply DC to deliver therapeutic modulation of the nervous system. This thesis is focused on the development of the µF that can be used to realize the function of FS which includes: a shape memory alloy (SMA) valve used to mechanically control ionic current in µF channel [24], [25]; an ionic transistor which can be used to non-mechanically control ionic current; an ionic current sensor used to measure the ionic DC output [26]; a proof of concept test for FS with a µF chip using SMA valves [21].

Chapter 2

Shape memory alloy valve

FS requires two actuators to actively control the ionic current in the µF chip shown in Figure 1.1. A mechanical µF valve [27], [28] needs to change its impedance to modulate passing ionic current by switching the valve state (open/closed states) to control ionic current in FS. The valve's actuation mechanism used in FS needs to be on-chip to accommodate the small size of this neural implant. Being a system open to target tissue, the µF of FS needs to be filled with solutions compatible with physiological electrolyte. With limited conductivity of the solution, the channel size of the µF was estimated to be ~1mm in diameter based on the design of the channel network in Solidworks such that it won't impose high impedance in the system which would require excessively high compliance voltages. Thus, the microvalve for FS needs to be able to control a ~1mm diameter channel which is larger than the channels (10-100µm in diameter) controlled by conventional microvalves. The switching duration of valve limits the frequency of

switching the electrodes between their charging/discharging states as the electrode should not flip its polarity before the valve switching to avoid interruption of the DC output shown as in Figure 1.1. On the other hand, the electrode must flip its polarity to discharge before exceeding its limited CIC to avoid electrolysis which requires the microvalve to be rapid in switching. For example, in the case of delivering 1mA via the electrode, the switching duration of valve estimated with poly(3,4-ethylenedioxythiophene) polystyrene sulfonate (PEDOT:PSS, 1mC/cm^2 in CIC) electrode with 1cm^2 surface area should be shorter than 1 second to avoid exceeding the CIC of the electrode. [10], [29]

With the understanding of constraints imposed by the FS design, we compared different published µF valve mechanisms and here we discuss their limitations. The existing valve actuation technologies are not suitable for the FS in terms of the size of actuator, implantability, switching speed, etc.

To begin with, pneumatic valves [30]–[32] regulate valve states by changing the gas or air flow into a chamber which requires an external apparatus to operate. Figure 2.1 shows an example of a pneumatic microvalve designed by Baek, J.Y. et al. [33] In this design, the elastomeric membrane can bend or relax to control the opening of a center hole between the inlet and outlet. The shape of the membrane (bending or relaxing) is controlled by the pressure of an air chamber on top of the membrane supplied by an external air pump. The limitation of pneumatic actuation is that it requires an external
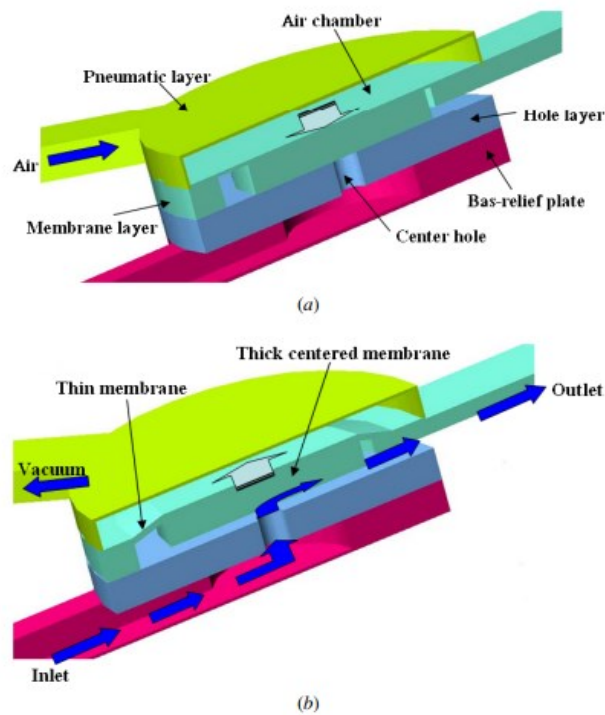
Figure 2.1 An example of pneumatic microvalve.

(a) The cross-section view of the pneumatic microvalve in its closed state. The air is pumped into the air chamber such that the membrane is pushed against the hole layer and blocking the center hole. (b) The cross-section view of the pneumatic microvalve in its open state. A vacuum is applied to the chamber which lifts the membrane and lets the fluid flow through from inlet to outlet. [33]

apparatus to supply the air pressure which is not suitable for FS in consideration of implantability.

Phase change microvalves regulate valve state by changing the phase of a working fluid thermally to induce volumetric change in a system. [34]–[36] Figure 2.2 shows an example of a phase change microvalve using FC 40 (3M, St. Paul, MN), a fluid ideal for a variety of phase change applications. [35] This design uses the volume change of FC 40 liquid with the temperature that can be controlled by turning on/off the embedded micro

heaters. The increased volume of this working fluid deforms a thin membrane to close the channel underneath and stop the fluid flow inside. The time spent to actuate this microvalve is 11sec with 37mW power supplied to the heaters which is too slow for the microvalve in FS. A shorter switching duration (0.125sec) has been achieved using paraffin wax as the thermally sensitive material by Feng et al. [34] However, this microvalve still suffers from its long off-switching duration (3.5sec) which is the time used to restore its initial valve state, due to the slow cooling driven by natural heat dissipation. The microvalves in FS need to be rapid in switching on/off within ideally 1 second. This rapid
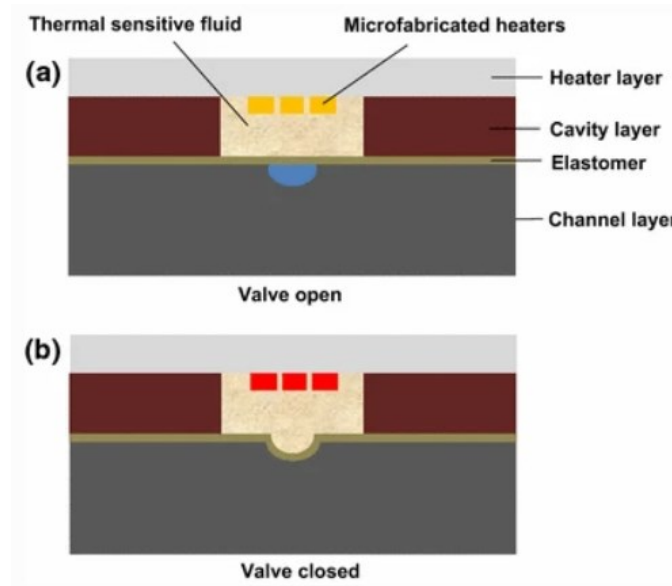
Figure 3.2 An example of phase change microvalve.

(a) The cross-section view of the phase change microvalve in its normal open state. The blue area is filled with fluid and wide open when the heaters are off. (b) The cross-section view of the microvalve in its closed state. The heaters are turned on and the thermal sensitive fluid expands in volume due to the increased temperature. The elastomeric membrane is deformed by the thermal expansion of the working fluid and curves down to close the channel. [35]

valve switching is necessary to reduce the required CIC of the electrodes and could benefit

the design of FS with smaller electrode size and higher DC output.

Piezoelectric and electrostatic microvalves regulate valve state by charging solid

material to induce electromechanical force. [37]–[39] Figure 2.3 shows an example of an

electrostatic microvalve that charges two electrodes to induce electrostatic force to open

the valve. [40] Upon the application of the activation voltage (V_{ac}), the two electrodes are

charged oppositely which induces an electrostatic force pulling the two electrodes toward

each other. As one of the electrodes is sandwiched in a flexible diaphragm, the diaphragm

will move along with the embedded electrode which creates an opening between the

stopper and the diaphragm. However, the microvalves using electric charge to activate

(piezoelectric or electrostatic) typically require relatively high driving voltage (from 50V

to 110V) to generate enough mechanical force for valve activation and could only provide
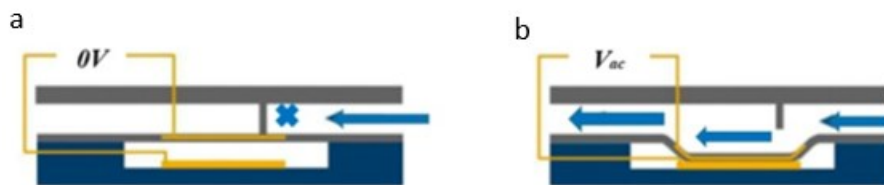
Figure 4.3 An example of electrostatic microvalve.

(a) The diagram of the electrostatic microvalve in its normal closed state. The blue arrow is the fluid flow blocked by the stopper. 0V is applied between the two Ti/Au electrodes (gold). One electrode is at the bottom of the bottom chamber. The other is sandwiched in a flexible diaphragm (grey) in the middle. (b) A high activating voltage (V_{ac}) is applied between the two electrodes to activate the valve to open. The diaphragm moves downward to the bottom electrode due to the electrostatic force between the two electrodes. [40]

up to 10μm displacement for the movable part of the valve. The high driving voltage and

small displacement are two clear disadvantages of these types of valves preventing their

applications in FS.

Additionally, electromagnetic valves use integrated solenoid coils to generate

electromagnetic force to control valves. [41]–[43] Figure 2.4 shows an example of an

electromagnetic valve. [43] In Figure 2.4a, the actuator contains a movable iron rod (5)

that can freely move up and down. Upon the application of a current through the winding

electric wire (3), the iron fixed (4) on the top applies a magnetic force attracting the

movable iron rod to move upward. A spring is attached to the movable rod that pulls it

back to its initial lower position when the actuating current is turned off. This vertical

movement of the rod can be used to control a microchannel. In Figure 2.4c, the valve is

in its normal closed state. The tapering tip of the movable iron pushes the PDMS
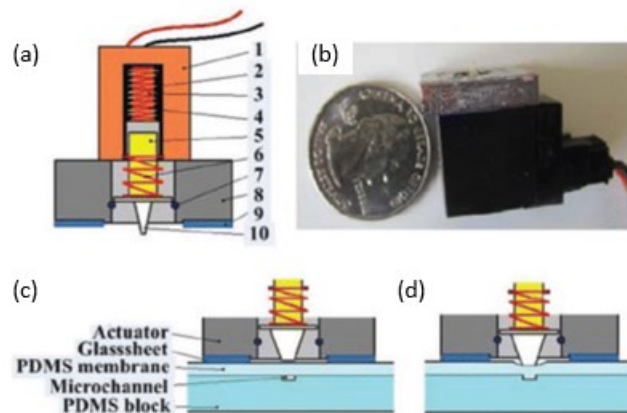
Figure 5.4 An example of electromagnetic microvalve.

(a) The diagram of the actuator part of the electrostatic microvalve. (b) A picture of the
fabricated microvalve. (c) The diagram of the valve in its open state after actuation. (d) The
diagram of the valve in its normal closed state. [43]

membrane to curve downwardly into the microchannel which blocks the fluid flow in the channel. After being activated (Fig. 2.4d), the moveable rod moves upward flexing the PDMS membrane and opening the channel. Electromagnetic valve is autonomous, and its actuator can be integrated into the controlled µF device. However, this type of microvalve is typically heavy and bulky due to the complex structure of the solenoid (Figure 2.4b) which is not an ideal valve solution for FS.

Shape memory alloy (SMA or Nitinol)-based actuation offers a potential solution for FS owing to its small size, rapid switching, and low actuating voltage. [44] SMA can transition between two different solid phases by heating and cooling. Since these two solid phases are different in crystalline structure, SMA will undergo reversible confirmational change with temperature which can be utilized to control a microvalve. For example, SMA can be manufactured into hair thin Nitinol wire which shrinks lengthwise upon electrothermal heating by passing electrical current through it. [45] This contraction of the Nitinol wire can be used to generate a pull force to reversibly open/close a microvalve. Pemble et at. were the first to use Nitinol wire for making a microvalve that pinches a 0.64mm inner diameter silicone tube to close. [46] The microvalve can open and close within 1-2.5sec but requires >300g actuating force due to the large diameter of the silicone tube. Similarly, Vyawahare et al. used a Nitinol wire to build a Polydimethylsiloxane (PDMS)-based microvalve. [47] Their device was used to control a 10-µm diameter channel by pinching the small channel but still exhibited 1.3sec off-to-on and 2.4sec on-to-off switching delays.

CHAPTER 2

To make a microvalve that can be used in FS, we designed a Nitinol wire valve using the plunger-membrane microvalve architecture [33] which was originally designed for pneumatic microvalves. Since the plunger-membrane microvalve requires very low force to operate, we estimated that we could operate this plunger-membrane microvalve with Nitinol wire to control a 1mm diameter channel within 1sec with small actuating force (<30g). We first characterized the designed valve in activating force, driving current of Nitinol wire, switching delays and open/closed impedances with short duration (~1min) or single operational cycle tests. Then, we operated the valve with one million open/close cycles to test its long-term reliability.

2.1 Microvalve design and schematics

We built a plunger-membrane microvalve using PDMS that can be actuated electrically with a Nitinol wire. Figure 2.5 shows a schematic representation with the cross-sectional views of the valve in its open/closed states. The microvalve is normally closed by a plunger blocking the vertical through hole channel when the Nitinol wire is inactivated. Upon the activation of the Nitinol wire with an electrical current passing through it, the wire is electrothermally heated and contracts thereby generating a pull force that lifts the plunger. Meanwhile, the elastic PDMS membrane serves as a spring and is stretched by the displacement of the plunger which generates a tension force that counterbalances with the pull force generated by the contracting Nitinol wire. By the continuous application of current through the Nitinol wire, the plunger can maintain at its lifted position and the microvalve is constantly open. Upon withdrawal of the electrical
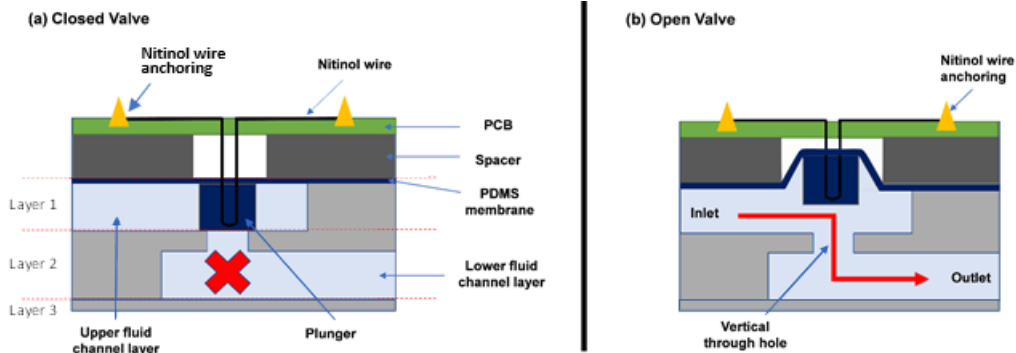
Figure 6.5 Microvalve design and schematics.

(a) Cross-sectional view of the microvalve in closed state. The layers 1, 2, 3 (light grey) delineate the PDMS layers bonded together that construct the upper and lower fluid channels (light blue). Layer 1 contains a thin PDMS membrane and a PDMS plunger (dark blue) attached on the membrane. The middle of the Nitinol wire is embedded in the plunger, and the two ends of the wire are anchored on a PCB (green). The red cross delineates that the channel is blocked by the plunger. (b) When the Nitinol wire is actuated electrically and shrinks lengthwise, the pull force generated by the wire lifts the plunger upwards thereby opening the microvalve and allowing an ionic current (red arrow) passing through.

current, the wire which is exposed to the air naturally cools down by losing heat to its environment and relaxes back to its original length allowing the stretched membrane to pull down the plunger to block the vertical channel. Since the heat exchange between the wire and its environment impacts the temperature of the Nitinol wire, the valve needs to be recharacterized for a different thermal condition.

As geometrical parameters play an important role in the function of mechanical microvalve we provide necessary geometrical information of the microvalve design. The upper and lower channels are 1mm deep and the through hole channel is 0.8mm in diameter to test the performance of the designed microvalve in controlling channels in

millimeter scale. The upper channel is 4 mm wide to fit the size of the cylindrical plunger. The Nitinol wire is 2.5cm long which is estimated with the designed 0.1mm vertical displacement of the plunger. The PDMS membrane is 0.1mm thick being flexible enough to be stretched by small actuating force while being able to generate enough force to effectively recover the position of the plunger.

2.2 Fabrication

First, the molds for shaping the three PDMS layers (Fig. 2.5) were designed with Solidworks and 3D printed (50μm resolution) with a photocurable black resin (B9R-2, B9Creations, South Dakota, USA). The printed molds were then rinsed thoroughly in an ultrasound bath filled with 70% alcohol to remove uncured resin on mold surface. The molds were then post-cured under UV light for 12 hours for further solidity. The molds after UV light treatment were placed on a 95 °C hot plate for 24 hours to eliminate the residue of the resin solvent that inhibits the curing of PDMS. A 10:1 wt% mixture of PDMS base and curing agent (Sylgard 184) was stirred thoroughly and was degassed in a vacuum chamber to remove air bubbles trapped in the mixture. Shown as in Figure 2.6a the prepared PDMS mixture was then poured over the treated molds which were then transferred onto an 85°C hot plate for PDMS curing. For the layer that contains the plunger-membrane structure, we embedded a Nitinol wire (50μm diameter HT, Dynalloy, Inc., Irvine, USA) in the plunger before PDMS curing. A Nitinol wire was firstly fed through a needle to create a wire loop at the needle tip. The wire loop was then carefully submerged in uncured PDMS mixture at the plunger. After the PDMS was cured, the wire
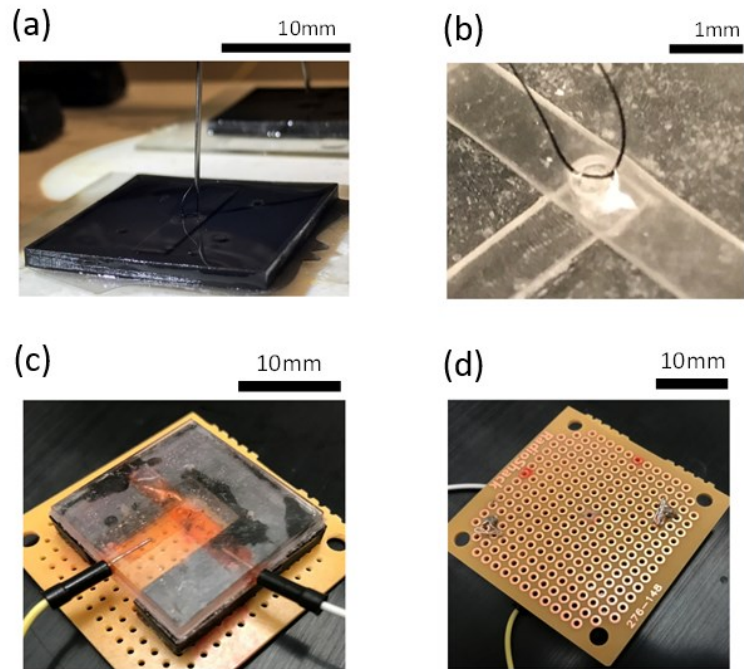
Figure 7.6 Images showing fabrication steps of the microvalve.

(a) The black mold is used to patten the PDMS layer with the plunger-membrane structure. The long needle is used to hold the Nitinol wire loop submerged in uncured PDMS mixture at the plunger location. (b) The three clear PDMS layers are bonded together after curing to create the valve channels with a cylindrical plunger blocking the vertical through hole channel at the center. The black Nitinol wire loop is embedded in the PDMS plunger which is attached to the membrane in the upper channel. (c) Two electrodes are inserted separately in the upper and lower channels of an assembled microvalve filled with red colored saline for testing valve impedance with electrical essay. The black spacer, positioned between the PDMS structure and the gold PCB, provides space for plunger to move vertically. (d) The two ends of the Nitinol wire are anchored on the backside of PCB.

loop was secured inside the PDMS plunger. The three PDMS layers were carefully peeled off, then were bonded together using corona treatment of PDMS to form the microvalve channels as shown in Figure 2.6b. In Figure2.6c the bonded PDMS chip was mounted on

top of a PCB with a black spacer between them which provides enough vertical space for plunger to move. Since Nitinol wire is not solderable, we fed the end of the Nitinol wire through a small copper tube which was then crimped hard to create a secured metal joint. The joint was then soldered on the backside of PCB (Figure 2.6d). The distance between the two joints was manually adjusted such that the Nitinol wire was slightly tensioned without pulling the plunger away from the blocking site.

2.3 Experimental setup

During operation of the microvalve, the impedance of the microvalve was monitored with an electrical assay. A 5V, 1kHz sinusoidal voltage was applied across the microvalve channel in series with a 56Ω sense resistor (Figure 2.7a) using a function generator (B&K Precision 4003A). Two electrodes were separately inserted in the upper and lower channels shown as in the image. The voltage across the sense resistor was monitored with an oscilloscope (Tektronix TPS2014B) and indicated the current passing through the microvalve. Thus, the impedance of microvalve was calculated by dividing the voltage between the two electrodes with the obtained current through the microvalve. The choice of Rs needs to consider the tested range of valve impedance. The test setup in Figure 2.7a is equivalent to a voltage divider constructed with the valve channel connected in series with the Rs. In this circuit, $V_{sense} = V_{in} * (\frac{Rs}{Rs+Rv})$ where V$_{sense}$ is the voltage signal measured across the R$_s$, R$_v$ is the impedance of valve channel, and V$_{in}$ is the AC voltage applied between the two inserted electrodes. Thus, the sensitivity (the change of measured voltage signal per unit change of valve impedance) of this impedance

(a)

(b)
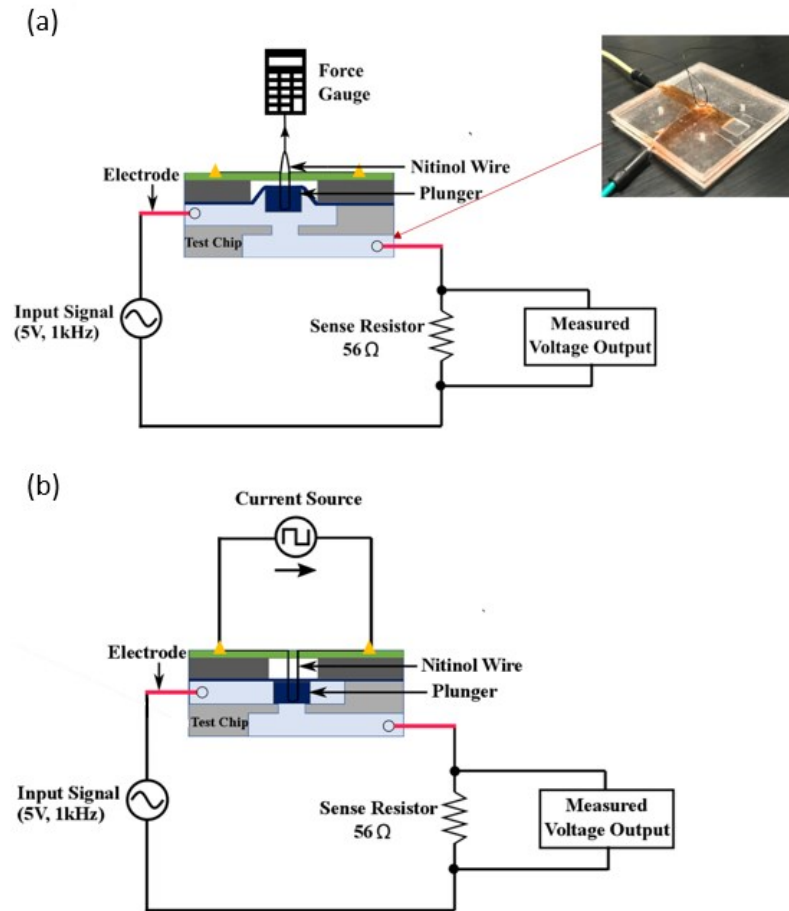
Figure 8.7 Experimental set-up.

(a) Diagram of the set-up that was used to measure the pull force required to switch the normally closed microvalve to open. The pull force was measured by a force gauge hooked with the Nitinol wire. The impedance of microvalve was measured by applying 5V, 1kHz sinusoidal voltage across the valve channel in series with a 56Ω sense resistor. Two electrodes were separately inserted in the upper and lower fluid channels shown as in the image. The voltage across the sense resistor was monitored with an oscilloscope. (b) Diagram of the set-up used to actuate the microvalve with a controlled direct current supplied by a current source connected with the anchored Nitinol wire.

measurement system is $\left|\frac{dV_{sense}}{dR_v}\right| = V_{in} * R_s * (\frac{1}{R_v+R_s})^2$. To evaluate the performance of

the setup with different R_s, we chose dV_{sense} >2mV which is the bound of random noise of

V_{sense} measured in this setup such that the signal-to-noise ratio (SNR) is >1. The dR_v is the

resolution of impedance and was chosen as 1kΩ considering the impedance range of the

designed valve. As calculated, when Rs is 56Ω, the SNR maintains >1 until R_v increases up

to 12kΩ. Then, the SNR decays to <1 with further increase in R_v. We selected R_s=56Ω to

test the kinetics of the valve's switching due to its high SNR (>10) during the valve's

opening (a few kΩ valve impedance). This high SNR allows us to observe the impedance

change with a better resolution (SNR=1 with 100Ω resolution). However, 56Ω Rs is too

small to be used to measure a high valve impedance (e.g., 20kΩ) due to its low SNR (e.g.,

0.34) in this case. We increased the Rs to 30kΩ to separately measure closed valve

impedance.

To optimize the pull force required to open the microvalve, we tested the microvalves

with different size of plungers. In these tests, the Nitinol wire was hooked to a force gauge

instead of being anchored on PCB (Figure 2.7a). The force gauge was fixed onto a manual

micromanipulator that controls vertical displacement of the plunger. The pull force

applied to the plunger was measured by the force gauge and can be controlled by

changing the vertical position of the force gauge with the micromanipulator.

To test the electrical actuation of the microvalve, the Nitinol wire anchored on PCB

was connected to a function generator (Tektronix AFG1022) that applies voltage pulses

through the Nitinol wire. The current through the Nitinol wire was measured by a digital

multimeter (FLUKE-115) and can be adjusted by changing the amplitude of the applied voltage.

2.4 Results and discussion

Optimization of pull force

The required pull force necessary to open the microvalve must be lower than 36g, the upper limit of the stretching tension applied to the Nitinol wire, to prevent wire breakage. The lowered pull force could also prevent degradation of mechanical strength of the PDMS bonding of the thin membrane and the connection of the Nitinol wire in the PDMS plunger. We identified plunger diameter and height as key parameters that impact the required pull force. To establish the relationship between pull force and valve impedance, we used the test setup in figure 2.7a to apply a constant pull force to valve plunger for ~1min and measure valve impedance throughout the test. Constant pull force was increased from 0g to 30g (1g resolution of force gauge) by increasing vertical displacement of plunger with micromanipulator. Within the tested range of pull force limited by 36g upper limit of Nitinol wire, we observed a steady relationship between pull force and valve impedance.

First, we tested the microvalves with different plunger heights of 0.9, 0.95, 1 and 1.05mm keeping the plunger radius constant at 1.2mm. Figure 2.8a indicates that the pull force needed to open the microvalve decreases with the decreased plunger height. For a plunger with a height of 1.05mm, the required pull force for a complete valve opening was found to be around 20g, whereas for the plunger height of 0.9mm, the force was

around 7.5g. This is because, in resting state, the membrane was tensioned more by a higher plunger therefore requiring a larger pull force to overcome the initial membrane tension. We also noticed that the plunger height of 0.9mm which is shorter than the 1mm upper channel height still achieved a valve closure in resting state. This is because the vertical through hole channel was fabricated with a pillar structure in the mold that levitated the PDMS surface around the pillar due to surface tension. As the valve needs to open and close as commanded, we chose 0.95mm over 0.9mm for plunger height to create a small tension in the membrane which prevented the microvalve from being unintentionally opened by small force from the environment such as hydraulic pressure.

To test the effect of plunger radius, we tested the microvalves with different radii 1.2, 1.4, 1.6 and 1.8mm, while keeping the plunger height constant at 0.95mm. The effect of the plunger radius on the valve performance is plotted in Figure 2.8b. The required pull
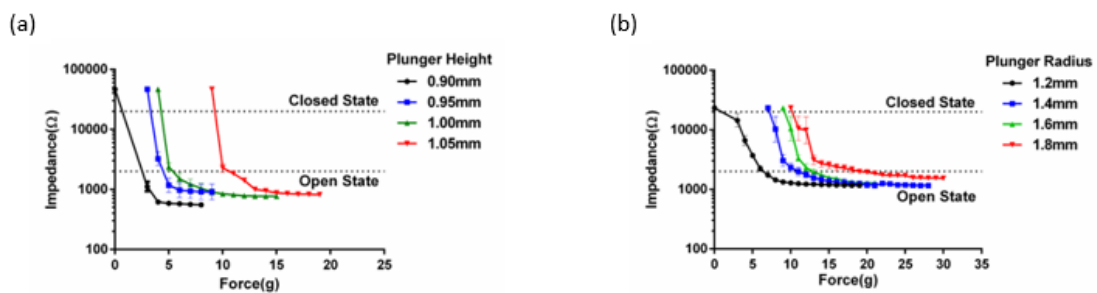
Figure 9.8 The force required to open the microvalve with different design of plunger.

(a) Force-impedance characteristic plot for plungers of different heights. (N=3, the number of tested valves) The top and bottom dotted lines represent the impedance of the microvalve in its closed (20KΩ) and open (2KΩ) states respectively. (b) Force-impedance characteristics plot for plungers of different radii. (N=3)

force increased with the radius of the plunger. At 1.2mm, the force required to fully open the valve was found to be around 10g, whereas for the radius of 1.8mm, it was around 20g. This is because the total planar area of this membrane-plunger structure is fixed, the larger the size of the thick plunger the higher the spring constant of this membrane-plunger structure which requires larger pull force to activate.

Based on these characterizations, we concluded that the height of 0.95mm and radius of 1.2mm were optimum parameters (i.e., requiring minimum force, while being able to fully open and close) for our subsequent electrical tests.

Actuating current

After the optimization of the pull force, we tested the electrical actuation of the microvalve with different electrical currents applied through the Nitinol wire. The duration of the applied current was set as 0.75sec which is within the ≤1sec switching
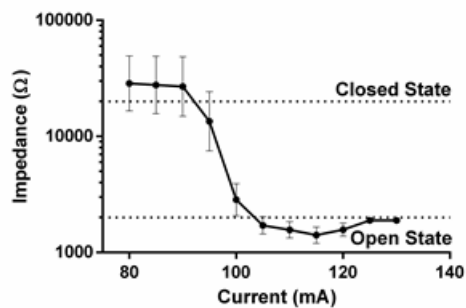
Figure 10.9 The effect of the amplitude of actuating current on closed-to-open switching.

Different currents were applied through the Nitinol wire for 0.75sec to open the microvalve. (N=3) The Y-axis is the impedance of the microvalve after the current was applied for 0.75sec. The top and bottom dotted lines represent the impedances of the microvalve in its closed (20KΩ) and open (2KΩ) states respectively.

duration requirement for the FS. The impedance through the microvalve was obtained by using the same electrical assay as shown in Figure 2.7b and used as an indication of valve states (open/closed states). Figure 2.9 shows the effect of the amplitude of the actuating current of Nitinol wire on the closed-to-open valve switching. The plot indicates that the actuating current with a duration of 0.75sec needs to be at least 105mA to reliably open the microvalve. This driving current is significantly lower than the driving currents (ranged from 200 to 400mA) required in the existing SMA microvalves. [46]–[48] As shown in Figure 2.9, using a driving current higher than 105mA doesn't benefit the valve performance with a lower open state impedance but exponentially increases the power consumption of the Nitinol wire.

Opening/closing delays

The opening and closing kinetics of the microvalve were tested by delivering 105mA actuating current with 50% duty cycle through the Nitinol wire. The valve impedance was tested by passing a 1KHz ionic alternating current (AC) through the microvalve and an example waveform of the testing AC in first on/off cycle is shown in Figure 2.10. The plot shows the time course of the ionic AC current flowing through the valve which was controlled by delivering a 105mA current through Nitinol wire with 0.75sec durations of current on/off. A time delay of $T_{on}=0.265$sec was observed from the point of the application of the actuating current to the point where the measured ionic AC starts to change. This observed time lag is due to the time required to heat up the Nitinol wire to its heating phase transition temperature (90°C). After being close to 90°C, the Nitinol wire

22
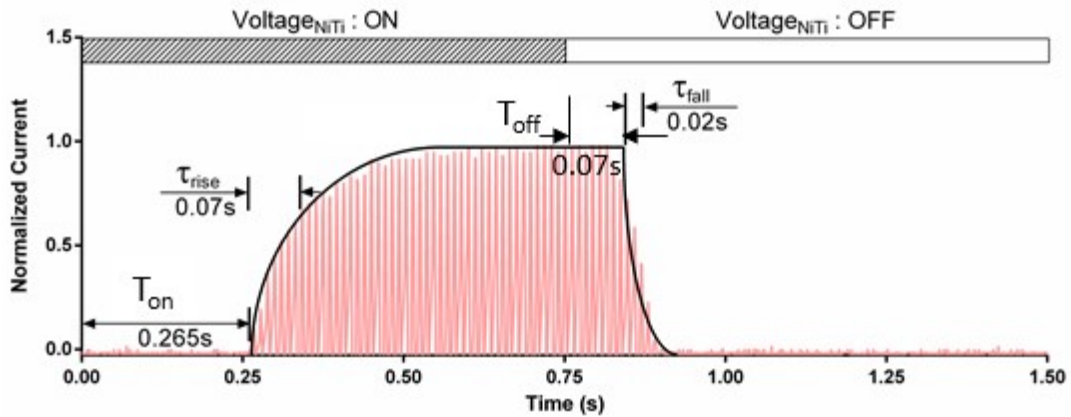
Figure 11.10 The opening and closing kinetics of the microvalve.

The red waveform indicates the amplitude of a 1KHz ionic AC passing through the microvalve under an ON/OFF operation described as the bar on the top. A 105mA actuating current was applied through the Nitinol wire from 0-0.75sec and was off from 0.75-1.5sec. The ionic AC passing through the valve was normalized with its amplitude when the microvalve was closed. T_{on} is the response delay of the microvalve after the onset of the actuating current. τ_{rise} is the time constant of closed-to-open switching. T_{off} is the response delay after the turn-off of the actuating current. τ_{fall} is the time constant of open-to-closed switching.

starts to contract rigorously which is accomplished with only a few degrees of further temperature increase. The time constant of this rapid wire contraction was found to be τ_{rise}= 0.07sec. The microvalve was maintained to be open to allow the ionic AC to pass through with the actuating current on. As the actuating current was withdrawn after 0.75sec, the measured ionic AC diminished to its baseline value reflecting the closed valve state. A response delay was observed from point of the current withdrawal to the point where valve starts to close, T_{off} =0.07sec. This response delay is due to the time required to naturally cool down the Nitinol wire to its cooling phase transition temperature (80°C). After being close to 80°C, the time constant for relaxing the Nitinol wire was found to be

τ_{fall} = 0.02s. The overall opening/closing delays for the tested microvalve actuated with 105mA current were 0.34sec and 0.1sec respectively.

The frequency of cyclic switching
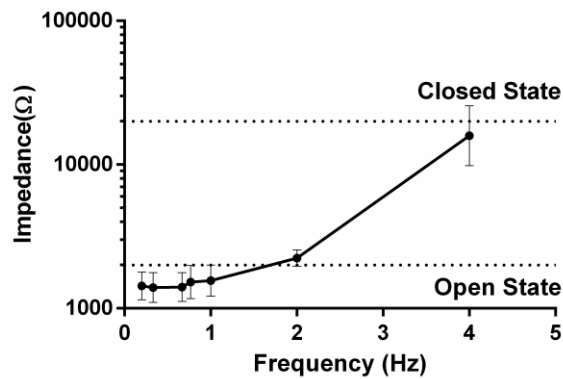
Figure 12.11 Performance of the microvalve cycled to open/close with different frequencies.

The Y-axis is the observed lowest impedance of the microvalve operated to open/close cyclically with 105mA actuating current in 50% duty cycle. (N=3) The top and bottom dotted lines represent the impedances of the microvalve in its closed (20KΩ) and open (2KΩ) states respectively.

As the microvalve has opening/closing delays due to heating and cooling processes of Nitinol wire, there would be a limitation on the frequency of cyclical operation of this microvalve that would impact the design of FS operation. Figure 2.11 shows the observed lowest impedance of the microvalve during a cyclical valve operation as a function of the frequency of the actuating current that was cyclically on/off. The amplitude and the duty cycle of the actuating current was set as 105mA and 50% while the duration of each cycle was varied. The valve failed to open and remained in its closed state for operational

frequencies ≥ 4Hz. For the frequencies in the range of 2Hz - 4Hz, the valve opened

partially. And for frequencies ≤1Hz, the valve could fully open. This observation of the

limitation on operational frequency could be explained by the required duration for the

heating of the Nitinol wire (0.34sec for 105mA actuating current). At high frequencies,

the duration of electrothermal heating were not long enough to rise the temperature of

Nitinol wire to its transition point resulting in absence of the displacement of the plunger.

Higher actuating current should be applied if the microvalve needs to be operated with

higher frequencies.

The closed valve impedance

As the setup in figure 2.7a is equivalent to a voltage divider constructed with the

valve channel in series with the Rs, the choice of Rs needs to consider the tested range of

valve impedance as discussed in the test setup. To accurately measure the closed valve

impedance, we increased the Rs to 30KΩ and tested six identical microvalves. As

measured, the closed valve impedances across all tested valves were 678 ± 102 KΩ.[21]

Long-term reliability

In this normally closed valve, a Nitinol wire breakage will lead the valve to fail to open.

Thus, we used the valve's open impedance as the indicator of valve's performance in this

long-term reliability test. Figure 2.12 shows the results of the long-term tests of the

microvalves operated with 105mA and 160mA actuating currents. Since the tested valves

varied in open impedance due to manual fabrication, the ACs passing through different

open valves can be different. To eliminate the impact of variation in open impedance and

focus on performance change over number of cycles, we normalized the AC in an open

valve with its baseline value measured in the first on/off cycle. As we characterized above,

105mA is the optimized value for actuating current while 160mA would overheat and

damage the Nitinol wire. In the plot, the ionic AC passing through the microvalve operated

with 160mA actuating current significantly decreased over the number of actuation

cycles. This degradation of valve performance was because of the overheating of the

Nitinol wire which degraded the mechanical strength of the wire and eventually led to its

break. For the optimized actuating current of 105mA, there was no appreciable change in

the performance of the microvalve for one million cycles.
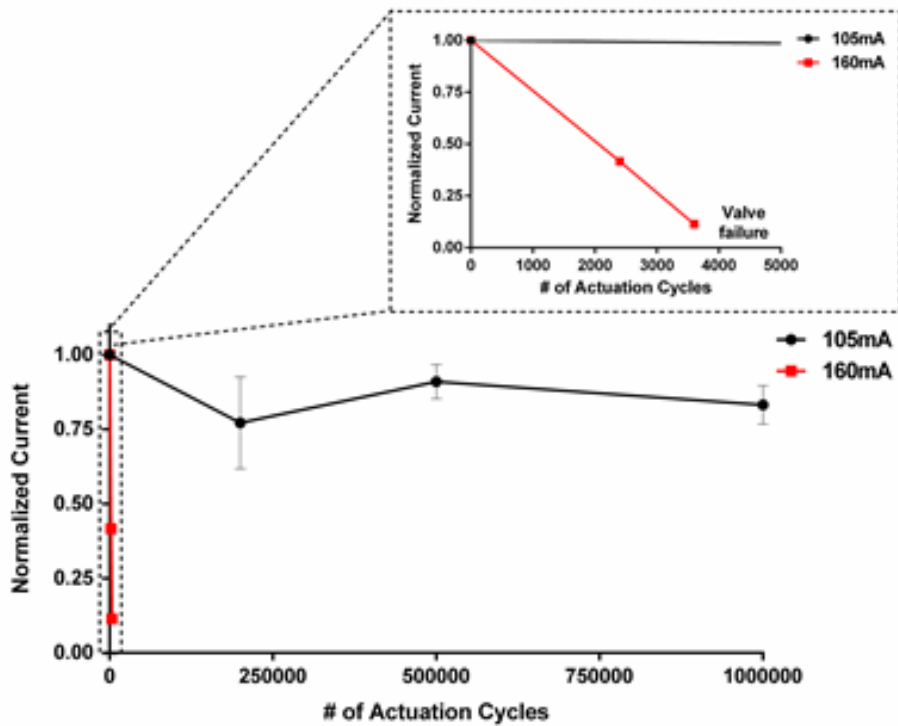
Figure 13.12 Long-term reliability.

The Plot shows the performance of the microvalve actuated by 105mA (N=2, black dots) and 160mA (N=1, red dots) actuating currents for many cycles. The duty cycle and duration of the operational cycle were set as 50% and 1.5sec. The Y-axis is the normalized ionic AC passing though the valve when the actuating current was applied through the Nitinol wire. The ionic AC was normalized with its baseline measured in an open valve.

Chapter 3

Ionic transistor

In chapter 2, we discussed the feasibility of using mechanical valves to control ionic current in µF and introduced the development of a microvalve actuated with Nitinol wire that could be used in FS. However, mechanical valves generate force to switch valve state which may lead to valve breakage (e.g., rupture of Nitinol wire and delamination of PDMS membrane, two major mechanical failures observed during our valve tests) if the applied force exceeds a threshold determined by the mechanical strength of valve structure. Additionally, the geometry (e.g., distance and angle) of valve structure can be changed by the deformation of its hosting µF chip (e.g., being stretched, compressed or bended) which impacts the performance of valve and could increase the risk of valve break.

Given these reliability concerns with mechanical valves, we explored ionic transistor, a non-mechanical alternative, that can be used to control ionic current in µF in a way that is analogous to its electronic counterpart. [49]–[52]

CHAPTER 3

Recently introduced nanochannel ionic transistors modify the electrical charge on the wall of a nanoscale channel to control ionic current. [53], [54] When the channel is small enough (in nanoscale) to be comparable to the thickness of electrical double layer (EDL), [55], [56] the resistance of ion transportation through the channel can be modulated with the surface charge on the wall. Figure 3.1 diagrams the effect of the surface charge on the inner channel wall over the ion redistribution in the channel. Due to electrostatic force, the charged channel surface will attract counterions and repel co-
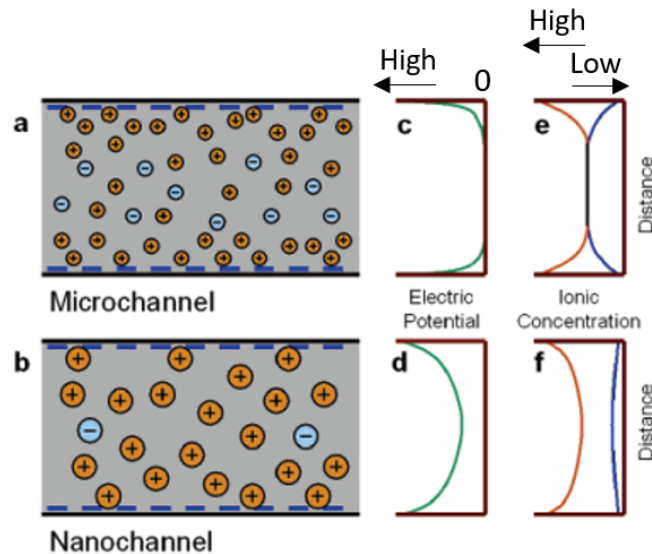
Figure 14.1 The effect of the surface charge in nano and micro channels.

(a) The diagram of the ion distribution in a microchannel with negative surface charge. (b) The diagram of the ion distribution in a nanochannel with negative surface charge. (c) The electric potential (green line) in the microchannel. The vertical axis represents the distance to the channel center. The horizontal axis represents the electrical potential. (d) The electric potential in the nanochannel. (e) The cation (orange curve) and anion (blue curve) concentrations in the microchannel. The vertical axis represents the distance to the channel center. The horizontal axis indicates the ionic concentration. (f) The ionic concentrations in the nanochannel. [48]

ions which induces the redistribution of ions in the channel. In a microchannel, the redistribution of ions is confined within the EDL at the surface of the inner channel wall without reaching deeper into the channel as the electrostatic force becomes weaker with the increase of distance. (Fig. 3.1a) Since most of the electrolyte in a microchannel remains neutral (Fig. 3.1c&e), the conduction of the microchannel for an ionic current passing through is not influenced. In the case with a nanochannel (Fig. 3.1b), the redistribution of ions induced by the surface change creates an EDL spreading throughout the whole channel space. The nanochannel is polarized (Fig. 3.1d) due to the uneven distributions of cations and anions (Fig. 3.1f) resulting in a strong influence over a passing ionic current by interfering with the electrical field. However, nanochannel ionic transistors have been shown to be functional only at low salt concentrations (e.g., 0.001M NaCl). [57] This is because the thickness of EDL decreases with the increase of the salt concentration. The deficient performance of the nanochannel transistors with physiological solutions (e.g., 0.15M NaCl) limits their applications in biomedical devices.

Ionic bipolar junction transistors (iBJTs) can function with electrolytes at biological ion concentrations. [51], [52], [58] iBJTs use cation selective (i.e., selectively block anion flow) and anion selective (i.e., selectively block cation flow) materials positioned adjacent to each other to create a basic component called bipolar membrane (BM) which is the ionic version of the PN-junction diode. [59], [60] The function of a BM is shown in figure 3.2a. A reverse bias current (a positive voltage is applied to the side with cation selective
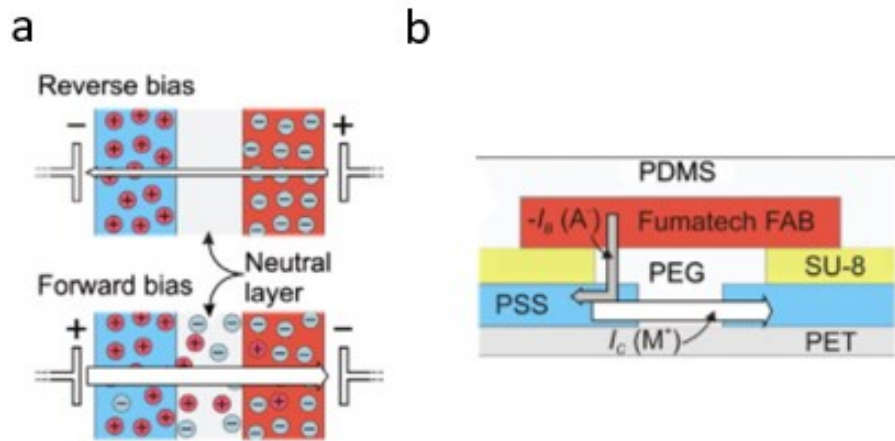
Figure 15.2 The schematic diagram of the iBJT.

(a) The diagram of a BM functioning as an ionic version of PN-junction. The blue block is cation selective material while the red block is anion selective material. The arrow indicates the ionic current passing across the BM. (b) The diagram of the iBJT. The red block is an anion selective membrane (AEM, Fumatech FAB). I_B are the control current delivering negative ions (A$^-$) to pass across the AEM. The grey arrow indicates the anion flow which is in the opposite direction of the applied I_B. The two blue blocks on the left and right sides are polystyrene sulfonate (PSS$^-$) that can transport cations (M$^+$) when a current (I_c) is applied. The white arrow indicates the cation flow which is in the same direction of the applied I_c. PSS are coated on a plastic polyethylene terephthalate (PET) foil (grey) and isolated from the AEM with SU-8 (epoxy-based negative photoresist, yellow). The white space at the center is filled with polyethylene glycol (PEG) hydrogel. The stack is sealed with PDMS. [52]

material) would deplete the mobile ions in the space between the anion and cation selective materials. Depletion of ions in the region increases the impedance causing the reduction of the ionic current passing across the BM. With a forward bias current applied (a positive voltage is applied to the side with anion selective material), mobile ions will accumulate in between the ion selective materials and the ionic current would be significantly higher due to the increased conductivity. Inspired by the electronic PNP

transistor in which one n-type material is doped with two p-type materials, an iBJT that

shares some similarities in structure has been developed by Tybrandt et al. to control

delivery of charged drug particles (i.e., ionic current) and is shown in figure 3.2b. A +10V

voltage is applied across the PSS-PEG-PSS from the left to right to deliver the I_c. In its cut-

off mode, both BM junctions (the spaces between the anion and cation selective

materials) are reverse biased with a +11V potential applied to the side with the anion

selective material. As I_B is depleting the ions in the PEG, I_c decreases with the increase of

the impedance of the PEG. By reducing the +11V potential to +6V, the BM junction on the

left side is forwardly biased such that the ions in the PEG are enriched resulting in an

increase of the I_c. This iBJT is designed to selectively deliver cations by this reversible

electrochemical reaction $PEDOT^0 + M^+:PSS^- \Leftrightarrow PEDOT^+:PSS^- + M^+(aqueous) + e^-$. The output

current (I_c) of this iBJT relies on the continuous supply of the aqueous M^+ produced from

the oxidization reaction of the limited $PEDOT^0$ which leads to a loss of performance of the

iBJT after being operated for a few minutes. [52]

   To be used in FS, an ionic transistor should be able to work with physiological

solutions (e.g., 0.9% NaCl ~ 0.15M NaCl) and maintain stable operation over long

durations. [61] To address these challenges, we developed an ionic transistor using ion

exchange membranes (IEMs). IEMs use ionic groups fixed in a polymer backbone to repel

mobile ions of the same charge (co-ions) and let through ions of different charge

(counterions). [62] The structure of this transistor is an ion-conductive channel

sandwiched by a cation exchange membrane (CEM) and an anion exchange membrane
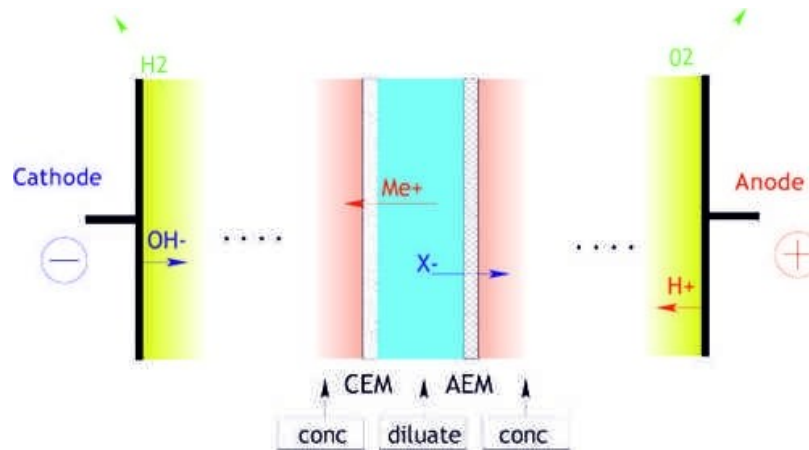
Figure 16.3 The diagram of an ED cell removing ions.

A voltage is applied across the ED cell composed of a CEM and an AEM, and a fluid channel sandwiched by the IEMs. As the ions move out of the intermediate space, the fluid in the region (blue) is diluted while the fluid at the external (red) is concentrated.

(AEM), similar to the construction of an electrodialysis (ED) cell used to remove ions from salt water. [63], [64] In figure 3.3, by applying a current across the IEMs, the ED cell continuously removes ions from the fluid flowing through the channel sandwiched by the IEMs. Using the same principle of operation, the ionic transistor is cyclically operated to deplete and enrich the ions in the static fluid filling the channel. In the transistor, the induced redistribution of ions changes the impedance of the channel, modulating an ionic current through it. The designed ionic transistor can impose a 10x impedance change in a channel filled with 0.9% NaCl solution and we observed stable operation of this ionic transistor throughout the test of 1000 cycles of on/off switching (160sec per cycle).

CHAPTER 3

3.1 Transistor design and mechanism

In Figure 3.4a, the ionic transistor consists of a sandwich structure of a cation

exchange membrane (CEM) (fumasep-fkb-pk-130, FuMA-Tech, Germany) (red) and an

anion exchange membrane (AEM) (fumasep-fab-pk-130, FuMA-Tech, Germany) (blue),

with a thin paper (grey) between them. The thin paper is filled with 0.9% saline and serves

as the ion conductive channel between the IEMs. The left side of the CEM and the right

side of the AEM are reservoirs filled with 0.9% saline such that an ionic current (I_c) can

travel perpendicularly across the IEMs to control the impedance of the channel. When I_c

is positive (right to left), the ions that flow toward the paper channel are blocked by the

IEMs while the ions that flow out of the channel are allowed to continue which depletes
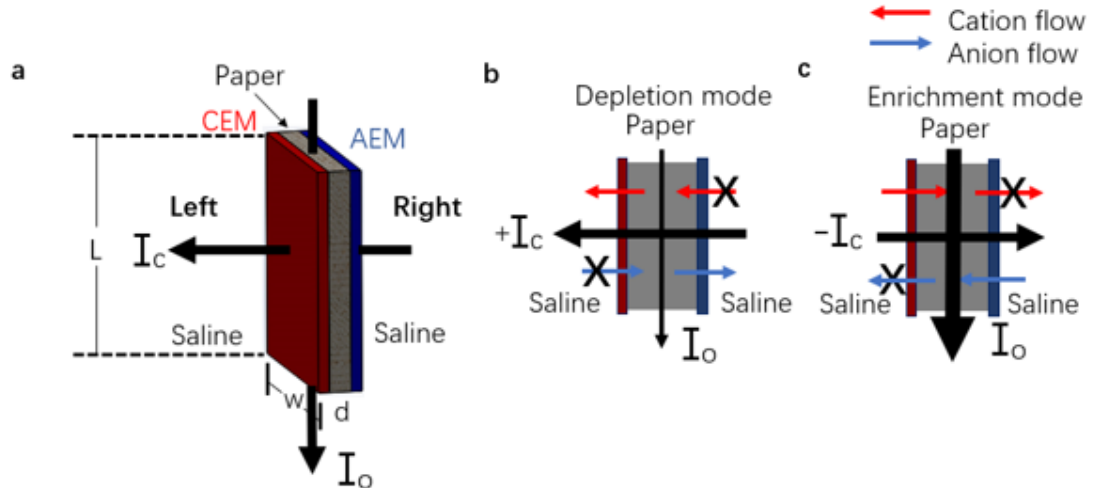
Figure 17.4 The design and mechanism of the ionic transistor.

(a) The structure of the ionic transistor with CEM and AEM. I_c is the ionic current that controls
the transistor. I_o is the ionic current that is controlled by the transistor. L (mm), w (mm), and
d (μm) are the dimensions of the paper channel (grey). (b,c) The ion flow during the depletion
and enrichment of ions in the channel. The thickness of the vertical arrow indicates (positive
correlation) the amplitude of I_o. "X" denotes the blocking effect of the IEMs over ion flow.

34

the ions in the paper channel (Fig. 3.4b). When I_c reverses its direction (negative: left to right), the ions flow into the paper channel to enrich it, while the ions that try to leave the paper channel are blocked by the IEMs (Fig. 3.4c). The paper channel can therefore switch between high ("off" state) and low ("on" state) impedances depending on its ion concertation controlled by I_c. This impedance change of the paper channel can be used to modulate an ionic current (I_o) passing along the same paper channel (Fig. 3.4b&c). Conduction for I_o is contributed to by not only the thin paper channel, but also by the IEMs and side reservoirs filled with saline. The conduction via the IEMs and side reservoirs is also modulated by I_c due to the ion concentration change on the surface of membranes.

3.2 Experimental setup

In Figure 3.5, the control current (I_c) was delivered via two carbon cloth electrodes positioned in the reservoirs filled with 0.9% saline and was supplied by a Keithley 6221 current source (Tektronix, Beaverton, OR) which can be programed to deliver certain control current (I_c) or apply a control voltage (V_c). The paper channel's impedance was monitored with the four-electrode measurement method diagrammed in Figure 3.5a. A testing current (I_{test}) was delivered via two Ag/AgCl electrodes and the voltage drop along the paper channel was measured with an isolated oscilloscope. The impedance was calculated by dividing the measured voltage with the amplitude of I_{test}.

Figure 3.5b diagrams the setup used to test the transistor function of controlling a ~1mA I_o. A constant voltage or a sinusoidal voltage with constant amplitude (AM system, model 2200) was applied to the paper channel such that I_o passing along the paper

channel would be controlled by the impedance of the paper channel. Since I_o is delivered via metal electrodes, its amplitude is impacted by the electrode impedance, which changes over time due to the complex electrochemical and mechanical processes around the electrodes. To eliminate this unstable factor impacting I_o, we used 40cm long stainless-steel wires (25 gauge) coiled and dipped in syringes to maximize the contact ($6.7cm^2$) of electrode/electrolyte, which significantly reduces the electrode impedance. Elimination of the impact of electrode impedance was verified by the observation of a
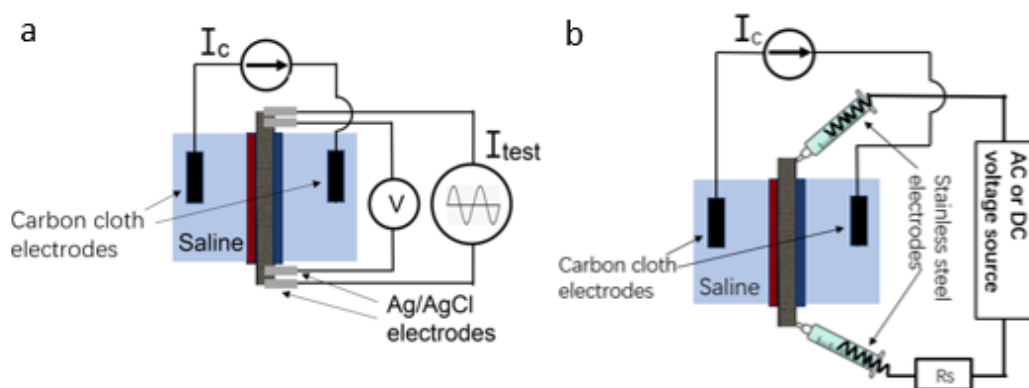
Figure 18.5 Experimental setup for testing the transistor.

(a) The setup that was used to characterize the impedance of the transistor. I_c was delivered via two carbon cloth electrodes (black) positioned in the reservoirs (blue) filled with saline. The impedance of the paper channel was measured with the four Ag/AgCl electrodes (silver). I_{test} was a 30μA sinusoidal current delivered to pass along the paper channel. The voltage drop along the paper channel was measured with an oscilloscope. (b) The set-up for delivering I_o (~1mA) being controlled by the transistor. I_c was delivered via two carbon cloth electrodes. I_o was delivered via two stainless steel electrodes positioned in two syringes filled with 0.9% saline that were in contact with the paper channel (grey). A sense resistor (R_s=2.1KΩ) was used to measure I_o.

constant I_o when a constant voltage (36V) was applied between the two stainless steel electrodes without the operation of the transistor.

3.3 Computational model

To visualize the redistribution of ions in the paper channel we created a computational model that calculates the ion concentration across the channel as a function of the duration of V_c. Even though the structure of the transistor implies a 1D system, we built a 2D model for the simulation of ion distribution in the channel to accommodate the cases with different aspect ratio (d/L) of channel space. The 2D model was based on diffusion equation of ions: $\frac{\partial c}{\partial t} = D * (\frac{\partial^2 c}{\partial x^2} + \frac{\partial^2 c}{\partial y^2})$ where c is concentration of ion, D is the diffusion coefficient of ion, and x and y denote locations inside of channel. Na^+ and Cl^- were assumed to have same diffusion coefficient of $1.6 cm^2/sec$ in the channel. The boundary condition for IEMs was an ion flux across IEMs (φ_{ion}) of which the rate was associated with I_c by this conversion equation: $\varphi_{ion} = \frac{I_c * C}{N_A}$ where N_A is the Avogadro constant and C is the number of ionic units of one coulomb charge. I_c was calculated with the applied V_c and the impedance across the IEMs that changed with ion depletion. This charge-to-ion conversion uses a unity current efficiency (the ratio of moles of salt removed to moles of electrons transferred) excluding the considerations of imperfect ion selectivity of IEMs, backward ion diffusion and bypassing control current. We intended to use this simple model to qualitatively understand the ion redistribution in the channel. For a more accurate model in the future, realistic values of current efficiency should be

obtained by experimental setup that can accurately quantify the removal of ions like the

ED cell. [65]–[67] The amplitude of the control current was calculated with the applied

control voltage and the impedance across CEM/paper/AEM sandwich structure that

changed with ion depletion. This impedance comprises IEM impedances, channel

impedance and the impedance across the electrodes and reservoirs. The impedances of

the electrodes and reservoirs are measured as 2KΩ in the experimental setup. The

channel impedance can be calculated with the ion concentrations at different locations

within the channel. The base impedances of IEMs are calculated with their specific area

resistances ($9\Omega \times cm^2$ for AEM, $5\Omega \times cm^2$ for CEM within 0.5M NaCl solution). The IEM

conduction is influenced by its lowest external NaCl concentration and thus needs to be

adjusted with the change of NaCl concentration. For low NaCl concentrations (<1M) the

membrane conduction decreases almost linearly with the decrease of external NaCl

concentration. [68], [69] The boundary condition at the midline of the space between the

IEMs was set as the first and second spatial derivatives of the ion concentration are zero.

3.4 Results and discussion

Thickness of the controlled channel

Because the number of ions in the paper channel is proportional to the thickness of

the paper (d), we hypothesized that d would have a major impact on transistor

performance. We monitored the impedance of the paper channel with different

thicknesses (d = 0.2, 0.1 and 0.04mm) over 60s after the onset of V_c =+40V. L and w were

kept constant at 14mm and 1.5mm respectively. In Figure 3.6a, the impedance of the
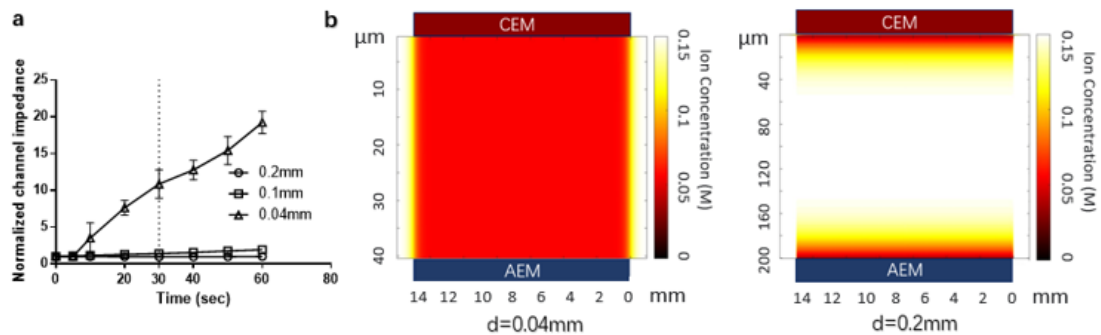
Figure 19.6 The impact of the thickness of paper channel.

(a) The experimental results of the impedance of the paper channel that was normalized with the initial impedance (~20kΩ at t=0) with different d (0.04, 0.1 and 0.2mm) (N=3, number of tested transistors). (b) The simulation results of the distribution of ions in the paper channel with d=0.04mm (left) and 0.2mm (right) at 30 seconds of ion depletion with V_c=+40V. The red and white colors represent low and high ion concentrations respectively.

paper channel with d=0.2mm did not change over time. Channels with d=0.1mm roughly doubled the impedance at 60s after V_c onset. Those with d=0.04mm increased 10.86 (±1.58) times at 30s then increased further to 19.25 (±1.26) times at 60s. However, a delay of the impedance change in response to the control input was observed in the first 5 seconds of ion depletion. This might be because the ion depletion initially takes place in close vicinity of the IEMs. The effect of ion depleting needs time to reach deeper into the channel via natural ion diffusion resulting in the delay of the impedance increase.

We created a computational model that calculates the ion concentration across the channel as a function of the duration of V_c. Figure 3.6b compares the ion distribution across the channel as the result of applying V_c=+40V to deplete the channel for 30s. If the channel is thick (d=0.2mm on the right), the ion-depleted region is focused on the edges

of the channel, leaving the middle section unaffected. The thin channel (d=0.04mm on the left) is greatly affected by the same V_c since the population of the ions in the thin channel is considerably less.

We conclude that the thickness of the paper is a major factor influencing the switching speed of the transistor in agreement with our hypothesis. This conclusion suggests the possibility for further operational speedup by reducing the channel thickness. However, the current design of the transistor is limited by the thinness of the paper commercially available. A thin layer coating of ion conductive material could be a potential alternative for achieving a thinner transistor channel in the future.

Control voltage for ion depletion

To understand the influence of the applied electric field on the switching speed of the transistor, we kept d at 0.04mm and tested with different V_c (+10, +20 and +40V) as shown in Figure 3.7a. We monitored the impedance of the transistor and normalized it with its initial value (~20kΩ at t=0). The normalized impedance reached 1.62(±0.28), 3.77(±1.1), and 11.27(±1.31) at 30s for V_c=+10V, +20V, and +40V respectively (Fig. 3.7b). The average time constant of the switching decreased from 96s to 54s with the increase in V_c. We chose V_c=+40V for the rest of the experiments setting the 10X change of the impedance within 30s to 40s as a reasonable performance goal.

With the measured I_c and the constant V_c, we analyzed the power supplied to the transistor for on-to-off switching and used the 10x impedance change as the desired switching performance to compare the power consumption with different V_c shown as in
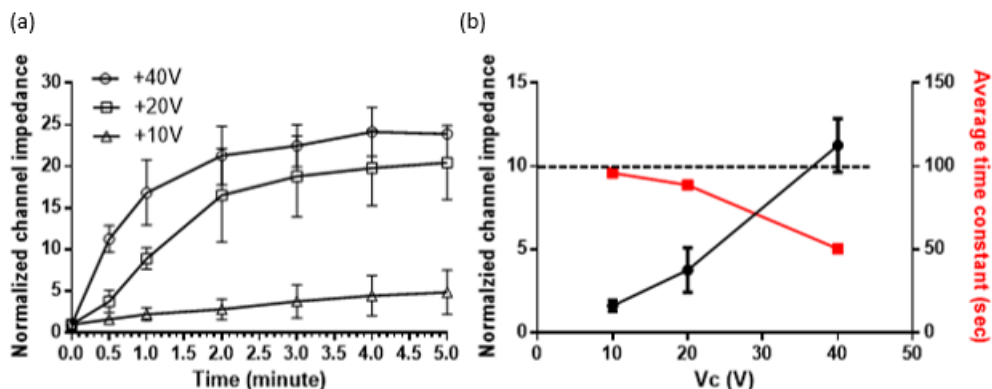
Figure 20.7 The impact of the control voltage.

(a) The time response of the normalized impedance of the paper channel with different V_c (+10, +20 and +40V) (N=3). (b) The normalized impedance of the paper channel at 30 seconds (black) and the average time constant (red) of the ionic transistor switching from on (low impedance) to off (high impedance) with different V_c (N=3). The black dashed line represents 10x change of impedance.

Figure 3.7a. In the case of V_c=10V, the transistor didn't achieve the 10x impedance change within 5 minutes. In the case of using V_c=20V for switching, the average power supplied to the transistor is 20.4mW with a switching duration of 78sec resulting in a total energy consumption of 1.59J. For V_c=40V, the average power is 122.2mW with a shorter switching duration of 24sec but resulting in a 2.9J energy consumption. The case with V_c=40V spent 2/3 less time to achieve the same 10x impedance change but consumed almost twice the energy comparing to the case with V_c=20V. We conclude that the choice of V_c is a trade-off between the switching speed and energy consumption of on-to-off switching for a same impedance increase. Other published ionic transistors are designed to control much smaller ionic currents (from 0.1nA to 0.2μA) and typically use a few μW

to operate. [50]–[52], [58] A high-flux ionic transistor has been reported to control 0.1mA ionic current with 1.6mW power supplied for device operation. [49] However, this reported transistor takes 600 seconds to switch its state resulting in ~1J energy consumption.

Backward diffusion of ions

When I_c=0 the channel was expected to maintain a constant high impedance in its off state. However, we observed a decrease of impedance over time when I_c was switched off to 0mA (Fig. 3.8, red dots). We reasoned that this decrease was likely due to backward ion diffusion driven by the difference of ion concentrations across the IEMs after the ion depletion. To prevent this decrease of impedance the system would need a depleting I_c to compensate for the backward diffusion of ions. We applied different small positive I_c (+0.04, +0.08 and +0.12mA) after the initial ion depletion to test this theory. For our
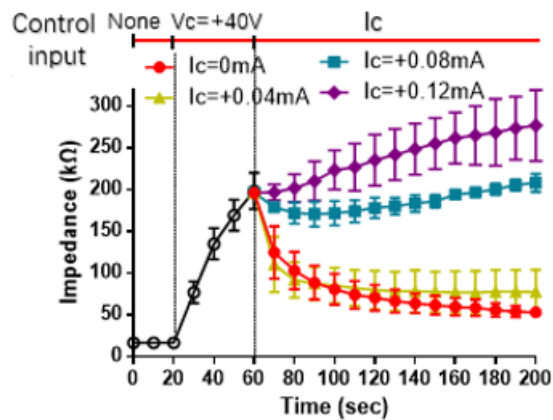
Figure 21.8 The impact of backward diffusion of ions and its compensation I_c.
The time response of the transistor that was tested with different compensation input I_c (0, +0.04, +0.08 and +0.12mA) after the completion of ion depletion at t=60s (N=3). The red bar on the top describes the timeline of the control input.

system, we found that we could obtain a relatively stable high impedance (160-220KΩ) with a compensating I_c=+0.08mA (Fig. 3.8, blue squares). The power supplied to maintain the off state with Ic=+0.08mA is ~0.24mW.

Control current for ion enrichment

We then tested the ability of the ionic transistor to cycle between on and off states. We first tried to cycle the ionic transistor by depleting the channel to turn it off, holding the high impedance, and then turning it on by simply allowing the impedance to decrease naturally without enriching current (i.e., I_c=0mA). Figure 3.9a shows the example waveform of the channel impedance when the enriching I_c=0 (e.g., 100s-140s). The low and high impedances in each cycle increased from 20KΩ to 79KΩ and from 205KΩ to 294KΩ respectively. Figure 3.9b shows the low and high impedances and their contrast
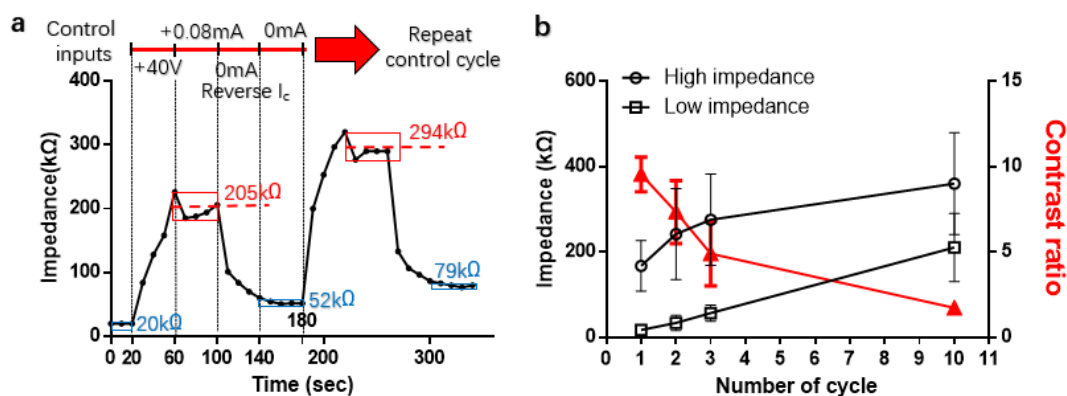
Figure 22.9 The impedance of the paper channel when the ionic transistor was switched on/off cyclically with enriching I_c=0mA.

(a) The example waveform of the impedance of the paper channel when the reverse I_c=0mA during the enrichment of ions (from 100s to 140s in the first cycle). The low and high impedances in each cycle are blue and red respectively. (b) The low and high impedances, and their contrast ratio (high/low impedance, red) over 10 cycles when the reverse I_c=0mA (N=3).

ratios (high impedance/low impedance) in the first 10 cycles. The contrast ratio decreased

from 9.5(±1) to 1.7(±0.1) due to the significant increase of the low impedance from 18(±6)

$K\Omega$ to 210(±65) $K\Omega$. The ionic transistor could clearly not fully restore its low impedance

within 40s unless we attempt to actively enrich the channel.

Since the ionic flux across the IEMs is associated with the charge delivered by I_c, we

hypothesized that delivering the same amount of charge backward ($Q_{enr} = Q_{dep}$) would

effectively restore the low impedance. Figure 3.10a shows the results when the negative

I_c during the enrichment of ions was applied to deliver the same amount of charge

backward for each cycle. In the first five cycles the low impedance maintained ~20$K\Omega$ but

the high impedance drastically decreased from 167(±20) $K\Omega$ to 53(±20) $K\Omega$ which still led

to a decrease of the contrast ratio from 12.4(±1.2) to 2.5(±1.1). The decrease of the high
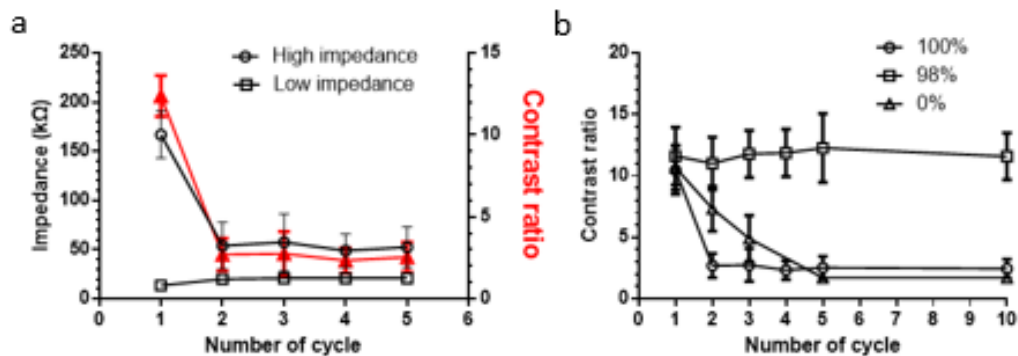
Figure 23.10 The contrast ratio of impedance of the transistor over the number of control cycles with different enriching I_c.

(a) The low and high impedances and the contrast ratio over 5 cycles when the reverse I_c was set to deliver the same amount of charge as depleting I_c in each cycle (N=3). (b) The contrast ratio over cycles when the reverse I_c (negative) was set to 0%, 98% and 100% of the forward charge injection of the depleting I_c in each cycle (N=3).

impedance indicates that the channel might be overly enriched. The actual number of depleted ions may be fewer than expected in theory. This phenomenon has been described as a loss of current efficiency in ED system which could be caused by the IEMs with imperfect ion selectivity, backward diffusion of ions driven by concentration difference and the current bypassing the effective IEM area. [70] This would suggest using $Q_{enr} < Q_{dep}$ to return the channel to its low impedance state. Figure 3.10b compares the contrast ratio over 10 cycles with $Q_{enr} = 0\%$, 98% and 100% of Q_{dep}. In this case, when Q_{enr} was at 98% of Q_{dep}, the contrast ratio maintained at 12.1(±2.9) over 10 cycles. We conclude here that the ionic transistor after being switched off (depleted) would require an enrichment current to restore its low impedance. The design of the enrichment I_c needs to consider the number of depleted ions corrected with a practical current efficiency.

Long duration operation of the transistor

Up until this point we have been characterizing the impedance change of the ionic transistor. Here, we investigated using the transistor to cyclically control 1mA ionic current (I_o) with the setup shown as in Figure 3.5b. Figure 3.11a shows the example waveform of a cyclically modulated I_o that was supplied by a 36V DC voltage source. I_o was modulated to change between 0.9(±0.1)mA (on) and 0.15(±0.05)mA (off). The contrast ratio between the high and low current was 6x which was smaller than the ~10x impedance change of the ionic transistor that we showed in Figure 3.10b. This occurred because the ionic current delivery system had a constant impedance of ~20KΩ due to the

Figure 24.11 The performance of the transistor in controlling an ionic DC.

(a) The ionic direct current (DC) I_o that was cyclically modulated with the transistor. The red bar on the top describes the control input. The reverse I_c=-1.16mA was calculated with 98% of the forward charge injection. The blue and red lines represent the amplitudes of the I_o after the transistor was switched on and off respectively. (b) The contrast ratio of the cyclically modulated ionic DC over 1000 cycles.

additional tubing (Figure 3.5b) which reduced the percentage change of the overall impedance. Figure 3.11b shows the contrast ratio of the delivered I_o over 1000 cycles. The contrast ratio was 5.4(±0.45) in the first cycle and 5.2(±0.4) in the last cycle.

Figure 3.12a shows the example waveform of an ionic alternating current (AC) that was cyclically controlled by the ionic transistor. Ionic AC was supplied by a 36V 100Hz sinusoidal voltage source (AM system, model 2200). Ionic AC was modulated to change between 0.95(±0.15) mA (on) and 0.2(±0.1) mA (off). Figure 3.12b shows the contrast ratio of the modulated ionic AC delivered at different frequencies. The average contrast ratio was 5.4 for ionic DC (red) and remained consistent up to the tested 500Hz. The blue line indicates the capacitive leak current associated with the test setup. The capacitive
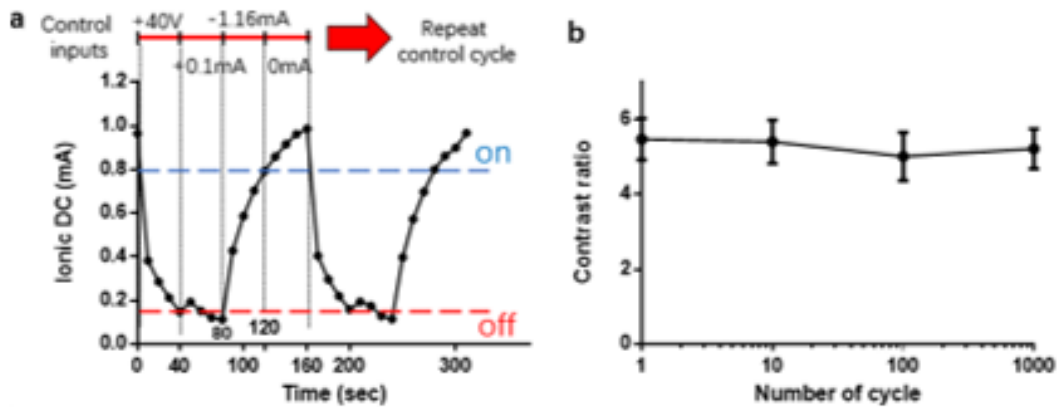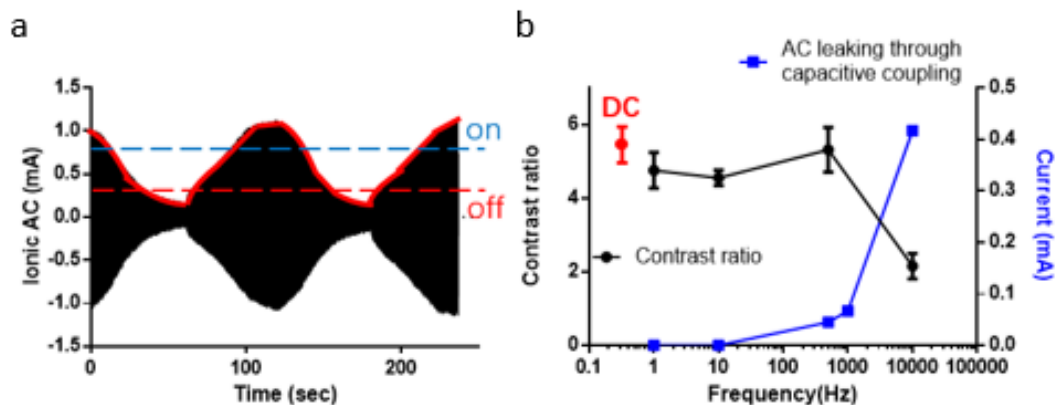
Figure 25.12 The performance of the transistor in controlling ionic AC.

(a) The ionic alternating current (AC) that was cyclically modulated with the transistor. The red envelope of the black waveform indicates the amplitude of the modulated ionic AC. (b) The contrast ratio (black line) for ionic AC delivered at different frequencies. The blue line is the AC capacitive leak associated with the test platform.

leak was measured by disconnecting one of the syringes from the paper channel. There was a 0.42mA capacitive leaking current at 10KHz within this disconnected system which is likely the cause of the significant decrease of the contrast ratio at 10KHz in Fig. 3.12b.

Chapter 4

Ionic current sensor

The working principle of FS is using two embedded µF actuators (e.g., microvalves or ionic transistors) to actively control the path of ionic current in a µF network such that the charge-balanced currents delivered via metal electrodes can be rectified into an ionic DC at its output. The FS can be seen as an ionic version of AC to DC bridge rectifier which rectifies AC input to DC output. [71] To maintain a constant DC output, FS requires a method to closely monitor the DC output (i.e., an ionic current) and adjust the current delivered by the electrodes if an error between the commanded and actual DC output is detected. This measurement of ionic current should be on-chip, rapid in response and accurate, and should work reliably for long durations. [10]

In a µF system that applies current via a single channel, the ionic current passing through the channel is stoichiometrically equal to the electronic current applied by the electrodes. In this case, the ionic current can be measured by using an electronic current

sensor connected in series with the electrodes. [47], [72], [73] However, that method cannot be applied to the FS due to its complex µF channel network that can route ionic current along different paths. In Figure 4.1 the delivered current (red arrows) will distribute through the discharge channel and the channel connected with the tissue. The distribution of current is based on the contrast ratio of the channel impedances which is changing during the operation of V1. Because of this changing current distribution, the ionic current output to the tissue cannot be reliably quantified with the electronic current applied thus, requires a sensor that can measure ionic current on-site in the output channel.

Ionic current is the flow of charged particles in electrolytes driven by electric field. Thus, the ionic current through a fluid channel can be calculated by dividing the voltage drop across the channel with the channel impedance. There are several emerging novel methods originally designed to monitor electric fields in electrolyte can be used to
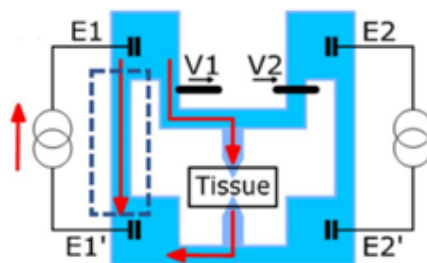
Figure 26.1 The µF of FS delivering ionic current to target tissue.

The channel network of the µF is filled with saline (blue). Current (red arrows) is delivered via E1 and E1' electrodes embedded in the µF chip. Microvalve 1 (V1) is open and microvalve 2 (V2) is closed. The ionic current delivered by E1 and E1' distributes through the output channel connected with tissue and the discharging channel (labeled with dashed lines) simultaneously.

quantify an ionic current passing through a channel. For example, imaging fluorescent voltage-sensitive molecules known as potentiometric dye are primarily used to detect neural activity in biology. [74] These molecules can change their spectral properties in response to voltage changes and generate electric field images with high resolution. [75] (Figure 4.2) However, that method requires an optical device to measure the spectral properties of the fluorescent molecules and is difficult to implement into the FS. Another example is an electroactive polymer (EAP) that can be used to recognize an electric field. [76] When stimulated with an electric field, the polymer will change its size or shape in accordance with the amplitude and direction of the local potential. However, the voltage recognizable to EAPs [15] is typically high (up to 1000V). Ionic polymer-metal composites (IPMCs), one emerging type of EAPs, are known for having low activation voltage (typically ~1V) but are slow in response (hundreds of milliseconds) to the activation voltage. [77]
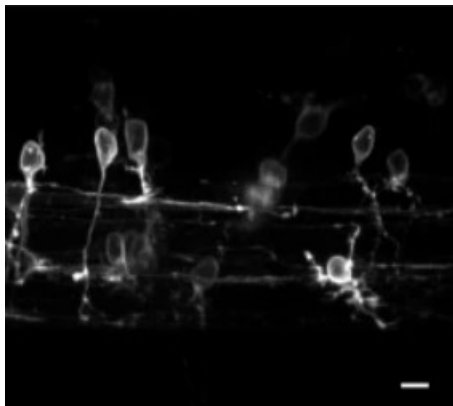
Figure 27.2 The voltage image of a spinal cord with Archon1-expressing neurons.
The brightness indicates the increase in fluorescence in response to neural activities. [75] Scale bar is 5µm.

CHAPTER 4

Using metal electrodes to measure ionic current could be a solution and has been widely adopted to detect biological activities such as electroencephalogram (EEG) and electrocardiogram (ECG). The ion flux traveling in electrolyte simultaneously induces a potential difference along the ion path, which can be transduced into a voltage signal with two metal electrodes probing two different locations along the path [78]. However, this method has been reported more as a method of event detection rather than quantification of current which lacks the investigation in its accuracy. Here, we present a detailed investigation of an ionic current sensor using Pt/Ir electrodes, originally proposed as a "current sensing element" (CSE) [20] that can be integrated into a μF device to measure ionic current.

4.1 Sensor design and mechanism

This sensor comprises two sensing electrodes and a voltage measurement circuit. The two electrodes are separately inserted into a target fluidic channel (Fig. 4.3). The ionic current passing through the target channel will simultaneously create a potential gradient along the channel. The potential gradient in electrolyte is established by redistribution of ions in the channel which leads to a difference of charge along the channel. By using two sensing electrodes to probe two different locations of the channel, the difference of the potentials (voltage) can be electrochemically transduced into a voltage signal that can be measured by a voltage measurement circuit. We chose Pt/Ir to be the electrode material owing to its high chemical/physical resilience. [29] The current used to test the sensors
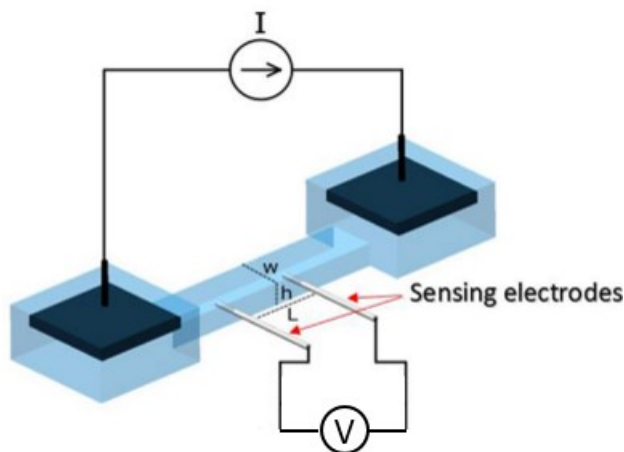
Figure 28.3 The diagram of the sensor probing a fluidic channel of a µF test platform.

The test platform is filled with saline (blue) and contains two reservoirs housing two carbon cloth electrodes (black) and a rectangular fluidic channel between them. ("w" is the width of the channel, "h" is the height of the channel) Two sensing electrodes (Pt/Ir) are inserted into the channel. ("L" is distance between the two sensing electrodes). The testing ionic current is supplied by a current source (Keithley 6221) through the carbon cloth electrodes. The two sensing electrodes are coupled with a voltage measurement circuit.

ranged from −50µA to+50µA with the required 1µA resolution based on previous therapeutic requirement. [10], [18], [19]

4.2 Fabrication and experimental set up

We used soft lithography and 3D-printed molds to fabricate the test platform (Fig. 4.3). The bulk of the test platform is a PDMS chip that has two separate reservoirs connected by a rectangular channel. The molds for different layers of the PDMS structure were printed by a 3D printer using photosensitive resin, B9R-2 (B9Creations, South Dakota). The structure layers were molded out of PDMS (10:1 ratio, 184 Sylgard elastomer kit, Dow Corning, Midland, MI). The test platform was constructed by bonding PDMS

layers after the surface treatment with corona discharge (BD-20AC, Electro-Technic products). The channel and reservoirs were then filled with 150 mM saline.

Figure 4.3 diagrams the structure of an embedded sensor (channel with two sensing electrodes) and the experimental setup. The sensing electrodes were made of uninsulated Pt/Ir wire with a diameter of 100um and were inserted into the channel to directly contact with the electrolyte inside. The effective electrode size was controlled by the depth of insertion of the Pt/Ir wire into the channel. Within the test setup, the testing ionic currents were delivered through two 1 cm*1 cm carbon cloth electrodes (CeTech Carbon Cloth with MPL-W1S1009, Taichung, Taiwan) separately positioned inside two reservoirs. The size of the carbon electrodes was chosen to be large enough to mitigate the effect of electrochemical reactions around the carbon electrodes during the assay. The testing direct currents (DCs) were supplied by Keithley 6221 current source. To test the sensor with alternating current (AC), we used a function generator (BK Precision, 4003A) to supply ionic AC through the channel.

4.3 The equivalent circuit model

The Pt/Ir electrode is a pseudocapacitive electrode [79] that can be polarized to change the voltage across the electrode/electrolyte interface which can be simplified as a resistor in parallel with a capacitor (Fig. 4.4). We hypothesized that this equivalent circuit model would be able to reveal the factors that would impact the performance of the sensor.
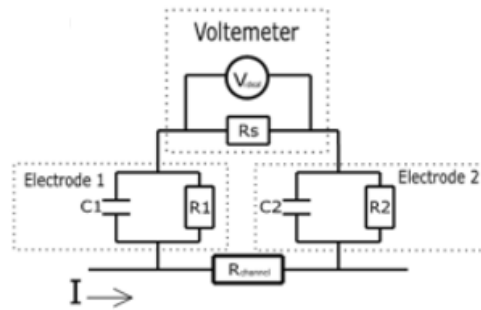
Figure 29.4 The equivalent circuit model of the sensor measuring an ionic current.

R1 and R2 are the electrode resistances. C1 and C2 are the electrode capacitance. R_s is the input impedance of the voltage measurement circuit. $R_{channel}$ is the channel impedance between the two electrodes. An ionic current (I) is passing through the channel. V_{cse} is the output of the voltmeter.

4.4 Results and discussion

The input impedance of the voltmeter

In our preliminary studies, we observed that when a multimeter (1MΩ input impedance) was used to measure the voltage between the two sensing electrodes, the measured voltage signal rapidly peaked upon the onset of a testing ionic DC then undesirably decreased over time (Fig. 4.5, black line). We hypothesized that this adverse sensing behavior is related to the low input impedance of the multimeter. As the input impedance is low being comparable to the electrode impedance, V_{cse} was significantly influenced by the effect of the voltage dividing between the voltmeter and the sensing electrodes. The gradual decrease of V_{cse} could be caused by the increase of the electrode impedance due to the formation of electric double layer (EDL) at the surface of electrode working. The electrode/electrolyte interface works as a resistor in parallel with a
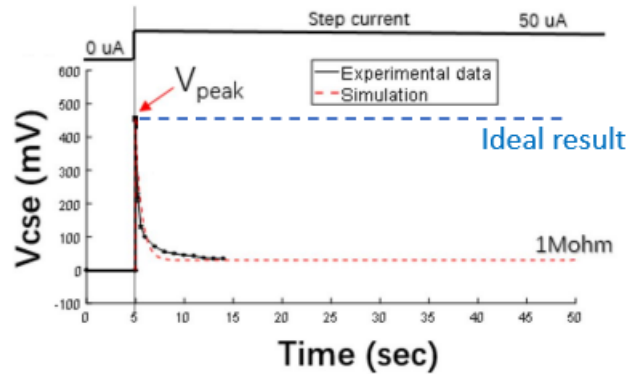
Figure 30.5 The response of the sensor using multimeter to measure a current step.

The V_{cse} in response to 50μA step current. V_{peak} is the peak value of V_{cse} upon the current onset. The black line represents the experiential result. The red dashed line represents the simulation result. And the blue dashed line shows the ideal V_{cse} response.

capacitor that can be polarized by delivering current through. This explanation of the decay of V_{cse} can be verified by using the equivalent circuit model. The circuit model can be reduced as shown in Fig. 4.6. Based on the model, a mathematical formula for the change of the V_{cse} after the current onset can be derived as $\Delta V_{cse} = V_{peak} \times (R1 + R2) / (Rs + R1 + R2)$. The formula indicates that the magnitude of ΔV_{cse} is related to the ratio
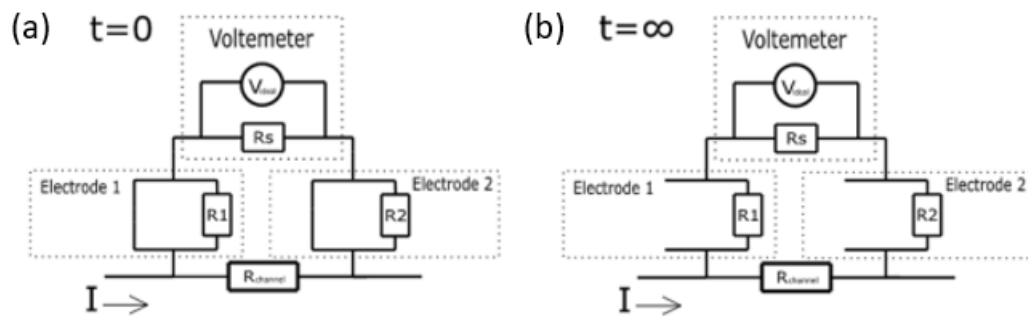
Figure 31.6 The reduced circuit models.

(a) The reduced model upon the current onset. (b) The reduced model after reaching a steady state.

between the electrode resistances (R1 and R2) and the input impedance of voltmeter (Rs). ΔV_{cse} decreases with increased Rs. To simulate the result with 1MΩ input impedance, we set R1=R2=5MΩ, C1=C2=0.8μF, $R_{channel}$=9KΩ and Rs = 1MΩ in the model. The simulation result is shown as the red dashed line in Fig. 4.5. As the model was able to duplicate the decay of V_{cse} observed in the experiment, we concluded here that the model adequately describes the cause of the adverse sensing behavior which is the low input impedance of the multimeter.

Based on the model, we estimated that using a voltmeter with a high input impedance could prevent the decline of V_{cse}. An instrumentation amplifier with a gain of 1 (INA121P, Texas Instruments, TX) was used to measure the voltage between the two sensing electrodes. The differential input impedance of the instrumentation amplifier was 1000 GΩ||1pF. The output of the instrumentation amplifier (V_{cse}) was recorded by a data acquisition unit (Micro1401-4, CED, Cambridge, UK). To explore the minimum input impedance required for a stable V_{cse}, we regulated down the input impedance by connecting a resistor (ranged from 10 MΩ to 10 GΩ) in parallel with the instrumentation amplifier to simulate for the situations with the input impedances ranged from 10 MΩ to 10 GΩ. Figure 4.7 shows the results of the ΔV_{cse} tested with a 50μA step current while varying the input impedance. We used the 2% error tolerance criteria based on the previously published biological experiments [3, 18, 19]. The experiment indicated that increasing the input impedance of the sensing circuitry would reduce the undesired ΔV_{cse}. The measurement error caused by ΔV_{cse} was below 2% when the input impedance was
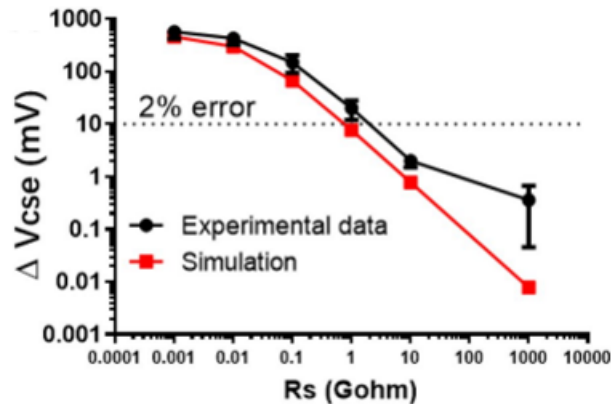
Figure 32.7 The impact of the input impedance.

ΔV_{cse} is the absolute change of V_{cse} from the onset of the testing current to the steady state of the V_{cse}. R_s is the input impedance of the voltage sensing circuitry. The black dashed line represents the ΔV_{cse} equivalent to 2% error from the base V_{cse}.

10GΩ. We simulated ΔV_{cse} with different input impedances using the same circuit model (Fig. 4.4). The simulation results (Fig. 4.7, red line) agreed with the trending of ΔV_{cse} with respect to R_s obtained with the laboratory experiments. In our system, 10GΩ was chosen as the required minimum R_s since both experimental and simulation results showed a ΔV_{cse} below the 2% error line with R_s=10GΩ. The associated ΔV_{cse} using an instrumentation amplifier with an input impedance of 1000 GΩ was 0.1 mV in simulation and was 0.36±0.26 mV in laboratory experiments.

Size of sensing electrode

In this experiment, we used the highest input impedance of the instrumentation amplifier (10^{12} Ω) for the best stability of V_{cse} and tested the impact of the surface area of the Pt/Ir electrode. We controlled the depth of insertion of the Pt/Ir wire into the channel to control the surface area of the electrode/saline contact. According to the experimental

result shown as in Fig. 4.8, the reduction of the surface area from 0.8106 to 0.0127 mm^2

did not statistically change the V_{cse} in response to a same DC. As calculated, a Pt/Ir

electrode with a surface area of 0.0127 mm^2 has a 5MΩ electrode impedance. Since this

electrode impedance is negligibly small comparing to the used 10^{12}Ω input impedance of

the instrumentation amplifier, the reduction of the electrode size didn't impact the V_{cse}.

Further reduction of electrode size may lead to a substantial increase of electrode

impedance thus may impact the V_{cse}. However, this hypothesis was not tested in this

study due to the limited precision of the control of surface area preventing further

reduction of the surface area. The error bars in Fig. 4.8 indicate the variance introduced

during the device fabrication. The channel size or the electrode distance can be slightly

different from the intended value due to the limited accuracy of the manual fabrication
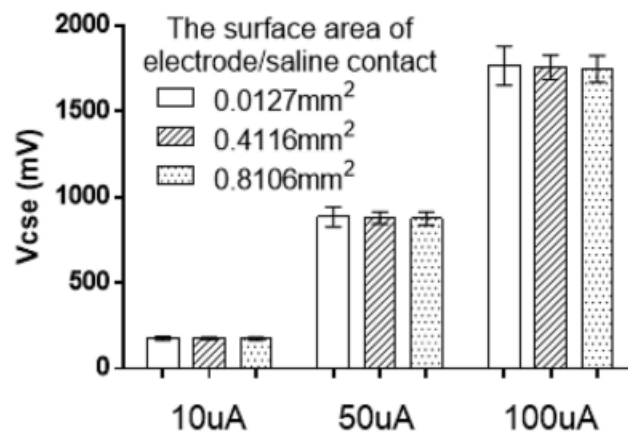
procedures.

Figure 33.8 The performance of the sensors using different surface areas of electrode.
V_{cse} in response to direct currents (10µA, 50µA and 100µA) with different size of the sensing
electrode which was quantified as the geometrical surface area of the electrode/saline contact
(N=3).

CHAPTER 4

The characteristic curve of the sensor

We delivered DC that ranged in amplitude from −50μA to+50μA with 1μA resolution to characterize the sensor. V_{cse} in response to DC inputs (N=3) was plotted to generate a characteristic curve establishing the relationship between the V_{cse} and the actual delivered ionic current (I_{act}). Thus, the reading of V_{cse} could subsequently be used to calculate the ionic current through the channel with the slope of the curve. We defined the sensitivity of the sensor as the change of the voltage signal (mV) per unit change in current (1μA). The sensitivity of the sensor depends on the impedance of the fluidic channel between the two sensing electrodes determined by the channel and electrode configuration. We characterized the sensors with rectangular channels with different cross-section areas (w*h, "w" and "h" are the width and height of the channel, respectively) and with different inter-electrode distances (L). The tested cases were described as L vs. w*h and were noted as S1 (5 mm vs. 2 mm*0.4 mm), S2 (10 mm vs. 2 mm*0.4 mm), S3 (10 mm vs. 2 mm*0.2 mm) and S4 (10 mm vs. 1 mm*0.2 mm). Figure 4.9a shows the characteristic curves for the tested cases. The slopes of the curves were 4.57±0.13, 9.36±0.23, 17.78±0.49 and 40.17±2.07(mV/μA, i.e., kΩ) for the S1, S2, S3 and S4, respectively (Fig. 4.9b). As we expected, the increase of L/(w*h) resulted in a larger channel impedance and thus proportionally increased the slope. We conclude here the sensitivity of the sensor is determined by the channel impedance between the two sensing electrodes. For a fixed channel dimension, the amplitude of V_{cse} can be improved by placing the two sensing electrodes with a longer distance (L).
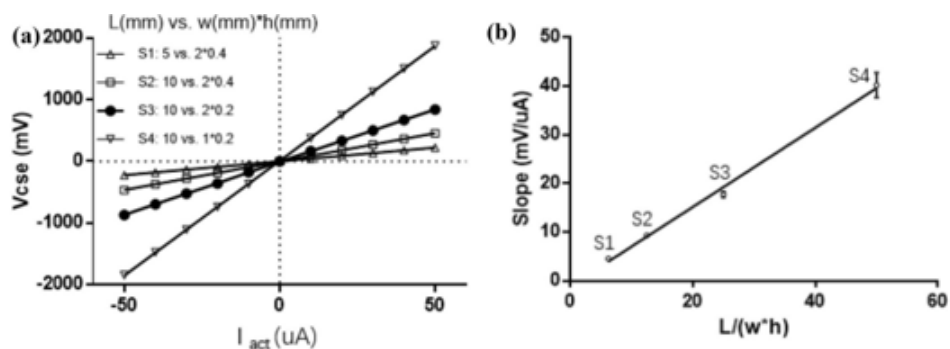
Figure 34.9 Characteristic curves (V$_{cse}$ vs. I$_{act}$) with different channel configurations.
(a) The characteristic curves of sensors (N=3) within different rectangular channels and with different sensing electrode distances. "w (mm)" is the width of the channel, "h (mm)" is the height of the channel, and "L (mm)" is the distance between the two sensing electrodes. (b) The slopes of the characteristic curves vs. L/(w*h) (N=3)

Signal-to-noise ratio (SNR)

Signal-to-noise ratio (SNR) is a standard way to quantify the level of random noise of a sensor. We defined the SNR as the change of voltage signal (mV) per unit change of the delivered ionic current (1µA) divided by the bound of random noise defined as 50% of the difference between the upper and lower limits of fluctuating voltage signal. We hypothesized that the random noise in the V$_{cse}$ is introduced by the electrochemical noise around the sensing electrodes [80] and is independent of the sensitivity of the sensor. We compared the SNRs of the sensors with different sensitivities that can be achieved by changing the channel dimensions (w*h) and electrode distances (L). In Figure 4.10 the SNR was shown effectively improved by increasing the sensitivity of the sensor. On the other hand, the maximum absolute value of noise bound of the V$_{cse}$ remained below 4.1
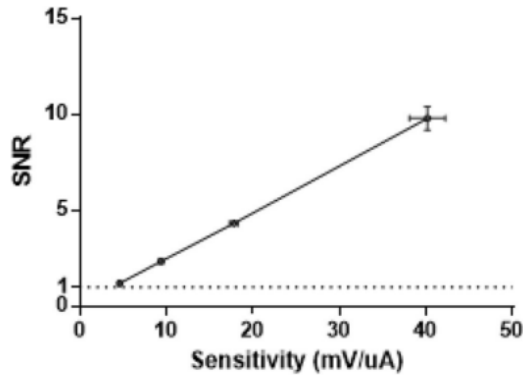
Figure 35.10 The SNR vs. the sensitivity.

The four different sensitives were achieved by changing the channel and electrode configurations. (N=3) The dash line represents a unity SNR.

mV for all tested cases and was independent of the delivered ionic current and the sensitivity of the sensor. A SNR of 1:1 satisfies the basic requirement of the SDCS with an error tolerance of±1µA.

The effect of temperature

An implanted device is likely to encounter small fluctuations in temperature. The typical human body temperature normally ranges from 36.5 to 37.5 °C but can reach to 41 °C in persons with fever. Variations in temperature may change the conductivity of the electrolyte in the sensor channel and alter the V_{cse}. We characterized the sensor under different environmental temperatures ranging from room temperature to human body temperature (20, 30, 37 and 40 °C degrees). We submerged the test device in a container filled with mineral oil to equally distribute the heat and then brought the system to the desired temperature with a heating plate. A consistent temperature was achieved by monitoring the reading from a thermocouple in the oil while controlling the heating rate.
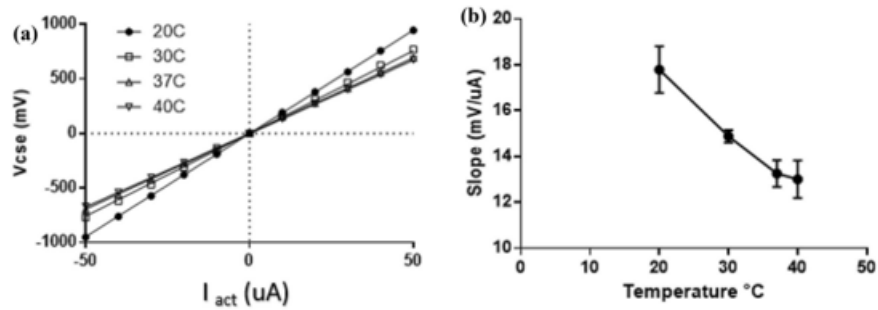
Figure 36.11 The effect of temperature (T).

(a) The characteristic curves of the sensors (N=1) under different temperatures. (b) The slopes of the characteristic curves vs. T (N=3) "N" is the number of tested sensors.

The shift of environmental temperature (T) changed the characteristic curve (Fig. 4.11a). Increasing T from 20 to 40 °C decreased the slope of the curve with an average rate of 0.24 mV/µA per Celsius degree (Fig. 4.11b). Applications that require a stable reading with a changing environmental temperature may therefore require a thermocouple to closely monitor the temperature. The slope of the curve can be calibrated with 0.24 mV/µA per Celsius degree difference in temperature.

The hysteresis of sensing

Hysteresis is the dependence of the state of a system on its previous state. It would be advantageous for this sensor to provide absolute measurements of the current that do not depend on the previous measurement. To test if the ionic current sensor is affected by its history of measurements, we first applied a baseline current (0µA, −50µA and+50µA) for 60 s. We then applied a step current (ranging from −50µA to+50µA) to see if the sensor response depended on the previous baseline. Figure 4.12 indicates that the
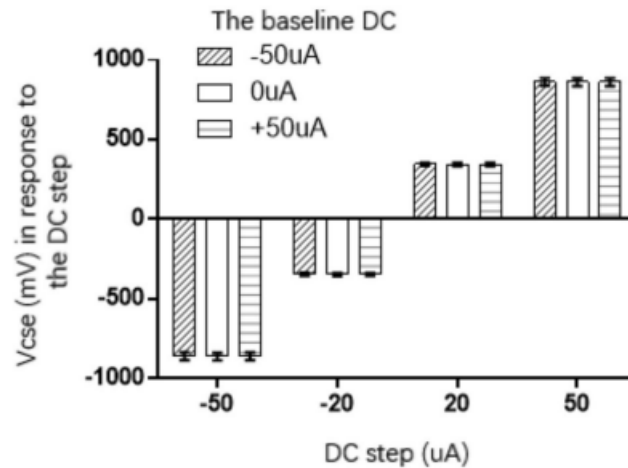
Figure 37.12 The sensor response to DC with different previous baseline current.

A DC step was applied after 60 seconds of a baseline current. (N=3)

V_{cse} of the sensor in response to the DC step was independent of the 60 s DC baseline.

There was no observed hysteresis effect on the sensor.

Sensor response to alternating current (AC)

The dynamic response of a sensor determines how fast a sensor can respond to an

input. We tested the dynamic response of the ionic current sensor with 100µA p-p

sinusoidal currents that ranged from 1 to 5 kHz (limited by our testing hardware). The

attenuation of the V_{cse} caused by the delay of the sensor's response indicates its limitation

in the speed to respond to a change of ionic current. The ionic current sensor reliably

measured AC signals within the tested range from 1 to 5 kHz (Fig. 4.13). When measuring

the 5 kHz signal, the gain of the V_{cse} was attenuated by 0.6%, and the phase was shifted

by −0.4 degrees with reference to the applied AC. We conclude that the sensor

measurement is stable up to the tested 5 kHz.
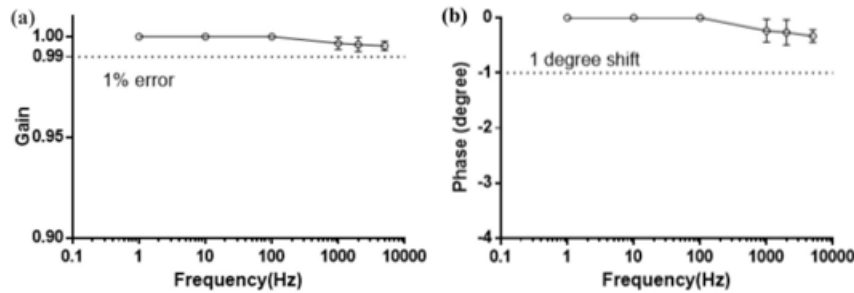
Figure 38.13 The bode plot of the sensor in response to AC.

(a) The gain bode plot for the amplitude of the V_{cse}. (b) The phase bode plot for the phase shift of the V_{cse} compared to the applied AC. (N=3)

Longevity

To be applied in biomedical implants (i.e., the FS), the performance of the ionic current sensor must be stable for long durations. A sensor with a changing performance over time needs to be frequently recalibrated to minimize its measurement error (i.e., the sensor error needs to be less than 1µA for the FS) which adversely interrupts the current sensing. To this point, we investigated the performance of the sensor continuously sensing ionic currents for one week.

To be able to test the sensor for one week, the testing platform needs to be modified to be suitable for long duration tests avoiding artifact that may impact the sensor performance. For example, the testing ionic DC was delivered via the carbon cloth electrodes embedded in the two reservoirs (Fig. 4.3) which unavoidably generates byproducts of electrochemical reactions. Consequently, the generated byproducts accumulate and diffuse through the fluid system of the testing platform and cause an impedance change of the sensor channel. To mitigate this artifact, we increased the total

volume of the two reservoirs to dilute the produced byproducts. We also applied mineral oil to isolate the system from air to prevent evaporation during the long duration experiment. Different total solution volumes (5 mL, 100 mL, and 1000 mL) in the two reservoirs were tested to verify the effectiveness of this method. We delivered a 50μA DC via the carbon cloth electrodes for one week and measured the channel impedance between the two embedded Pt/Ir electrodes every 24 hours. A conventional four-electrode method [81] was used to measure the channel impedance. In Fig. 4.14, 5mL solution volume resulted in a 40% reduction of the channel impedance after one week while 100mL solution volume ended up with a 20% reduction of the channel impedance. The case with 1L solution volume maintained the channel impedance within ±2% change for one week. This result agreed with the hypothesis that the electrochemical reactions

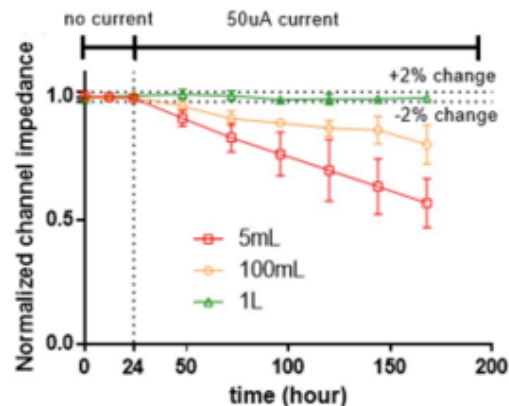**Figure 39.14 The artifact of a reduced channel impedance caused by the electrochemical reactions at the current delivery electrodes.**

The channel impedance was normalized with its initial value (~40kΩ in S4 sensor channel). A 50uA current was delivered to test the stability of the channel impedance. Different solution volumes (5mL, 100mL and 1L) of the electrode reservoirs were tested. (N=3)

around the current delivery electrodes could cause a significant change of the impedance of the sensor channel. This undesired artifact can be mitigated by increasing the solution volume of the electrode reservoir.

After eliminating the artifact that may impact the sensor performance, we tested the sensors (N=3) to continuously monitor a 50μA DC over a week of use. The sensors were characterized every 24 hours by sweeping the delivered current steps from −50μA to +50μA with a 1μA resolution. Since the characteristic curve (V_{cse} vs. I_{act}) was closely linear, we quantified the change of the curve as the change of slope and offset (y-intercept of the curve) as a function of time. We also added a negative control by connecting a 1GΩ resistor to the sensing electrodes such that the input impedance of the sensor was significantly reduced. The shunting current via the 1GΩ resistor could increase the rate of electrochemical reactions at the sensing electrodes and lead to impedance change of the sensor channel. During the characterization of the sensor with the sweeping current, the 1GΩ resistor was temporarily removed from the circuit.

We fabricated and used the sensors with an average sensitivity of 40 mV/ μA (S4 sensor channel) throughout the longevity tests. Figure 4.15a shows the sensor measurement when converted to current (I_s in green). This result correctly reflected the actual delivered current (50μA, I_{act} in black) with an error less than 1μA over a week-long test. The slopes of the curve (V_{cse} vs. I_{act}) remained within the allowed 2% margin throughout the test in Fig. 4.15b1. The change of the offset of the curve (V_{cse} vs. I_{act}) was less than the voltage change that would cause a 1μA change in the sensor reading (Fig.
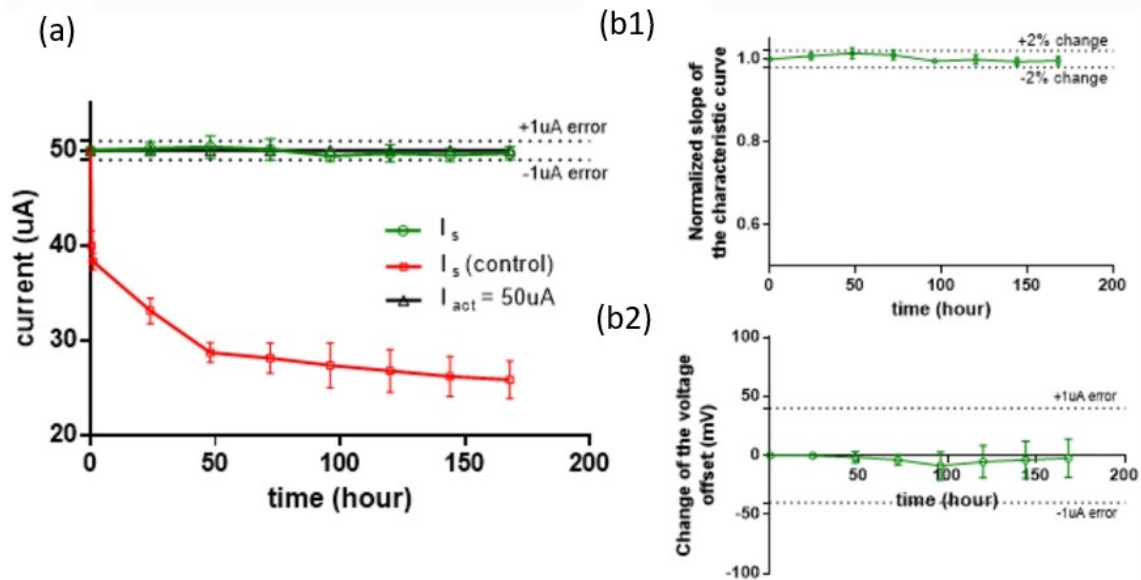
Figure 40.15 The longevity test of the sensor.

(a) The reading of current by the sensor (I_s in green) over time when the actual delivered current (I_{act} in black) was 50μA DC. The negative control (red) was conducted with a 1GΩ resistor connected in parallel with the sensor. (b1–b2) The slope and the offset of the characteristic curve (V_{cse} vs. I_{act}) of the sensor in use of measuring a 50μA DC over time.

4.15b2). In the negative control, we see an increased error over time if the 1GΩ resistor was connected to the sensor (Fig. 4.15a). The growing error in the control experiment may be caused by the electrochemical reactions at the sensing electrodes due to the small current leak via the 1GΩ resistor.

Chapter 5

Microfluidic chip of freeform stimulator

Up to this point, we have introduced the development of the μF components (i.e., Nitinol wire microvalve, IEM transistor and ionic current sensor) that could be used to realize the rectification of ionic current in the FS as is shown in figure 1.1. In this chapter, we use these designed μF components to build a μF chip for the FS. Both the Nitinol wire valve and the ionic transistor are actuators designed to actively control ionic current. To choose a proper actuator for the FS, we compared their performance in terms of operational voltage and switching speed. The ionic transistor using IEMs showed reliable modulation of ionic current, but the current design requires 40V operational voltage and 30 seconds duration to switch the transistor states. In contrast, the normally closed Nitinol wire microvalve presents a reasonable switching performance with a closed-to-open switching duration of 0.34s, an open-to-closed switching duration of 0.1s and an operational voltage of 2V. As we explained in the beginning of chapter 2, a rapid switching

would reduce the required size of electrode which benefits the miniaturization of the FS. Considering the switching speed and the operational voltage, we chose the Nitinol wire microvalve for the design of a benchtop FS. To maintain a constant DC at the output, we also developed the ionic current sensor to measure the DC output in real time and guides the FS to adjust its current delivery through the electrodes if an error between the commanded and actual DC output is detected.

We embedded two Nitinol microvalves, one ionic current sensor and four current delivery electrodes into a single µF chip constructed with PDMS. The µF chip was then operated to test the AC to DC rectification of the FS. To realize the current rectification, the control of the microvalves needs to consider the switching delays originated from the heating and cooling processes of the nitinol wire. Otherwise, the output of the FS would experience transient current dropping due to the loss of control over the output when both valves are closed at the same time. Figure 5.1a shows the diagram of the FS operated with two states (states A and B) when valve delays are not considered. The valves are driven with 50% duty cycle (i.e., the driving currents are turned on for 1.1s and off for 1.1.s when the duration of one cycle is 2.2s). In State A, valve 1 is open and valve 2 is closed. The current is driven by an independent current source from electrode E1 to electrode E1' through the tissue from top to bottom (red arrows) while electrodes E2 and E2' are discharged (black arrows) by another independent current source. In State B, valve 1 is closed and valve 2 is open. Instead, the current through the tissue is driven in the same direction via electrodes E2 and E2' (red arrows) while electrodes E1 andE1' are
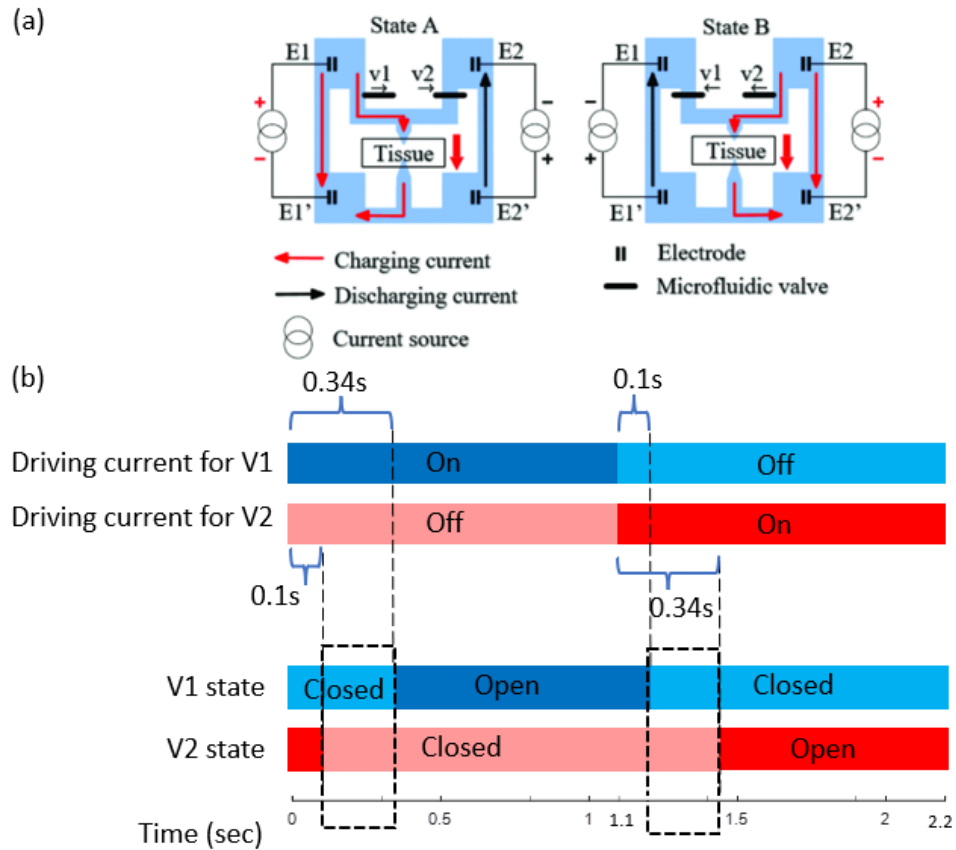
Figure 41.1 The FS operated with two states.

(a) Two continually repeating states of the same FS. To deliver a unidirectional current through the tissue, valves 1 (v1) and 2 (v2) open and close while two independent current sources deliver ionic current in sequential phases between electrodes E1 and E1' and then between E2 and E2'into channels filled with saline (blue). (b) The estimated valves' states in one operational cycle when the valve delays are considered. The driving currents for the V1 and V2 with 50% duty cycle are shown on the top bars with the closed-to-open (0.34s) and open-to-closed (0.1s) switching delays labeled. The corresponding valves' states are shown at the bottom bars. The durations when both valves are closed are labeled with squares with black dashed lines.

discharged (black arrows). Then the system state reverses from B to A again. In this way the electrodes are charge-balanced due to the periodically alternated charging and discharging while the output remains as a constant DC. However, in a realistic FS

operation the valves present switching delays. Figure 5.1b shows the estimated valves'

states when the valve switching delays are considered in the operation with the two

states. As characterized in chapter 2, the normally closed Nitinol microvalve delays ~0.34s

to open and ~0.1s to close. Due to these switching delays, a 50% duty cycle of the driving

current for the microvalves would lead to short durations when both valves are in closed

states (Figure 5.1b, black squares with dashed lines). Consequently, the FS will lose the

control over the ionic current at its output when both valves are closed. To avoid the

interruption of control over the output, we designed a control cycle for the microvalves

that takes into consideration the valve delays. We then operated the μF chip with the

designed control cycle and achieved the AC to DC rectification of the FS.

5.1 Fabrication of the μF chip

The microfluidic system is a three-layer PDMS structure. The mold for each layer as

shown in Fig. 5.2 was designed with CAD (Solidworks, Waltham, MA) and printed with a

3D printer (B9Creations v1.2, Rapid City, SD) using photopolymer resin (B9R-2-black,
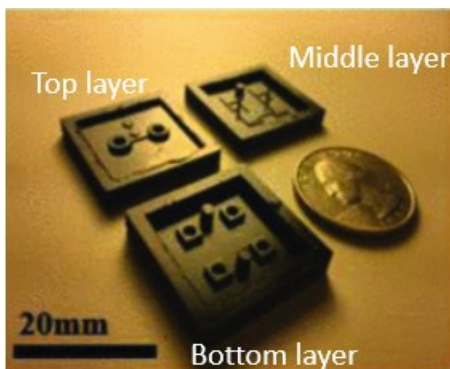
Figure 42.2 The molds for the three PDMS layers that construct the μF chip.

The μF chip is 2cm*2cm constructed with 3 layers of PDMS molded with these 3D printed
structures.

CHAPTER 5

Rapid City, SD). The printed molds were rinsed thoroughly with soap water in an ultrasonic

cleaner (Cole-Parmer 8891, IL) to remove uncured resin, until the mold surface became

glossy. The molds were then placed under water to avoid thermal stress and exposed to

UV light for up to 2 hours to be further solidified. Finally, the molds were baked on a

hotplate at 95℃ for 24 hours to evaporate moisture and resin base that can interfere with

PDMS curing.

We used Sylgard 184 (Dow Corning, Midland, MI) for fast prototyping of the PDMS

chips. Sylgard 184 is not reported suitable for medical or pharmaceutical uses and will be

replaced by medical grade silicon elastomer for clinical trial. PDMS monomers and curing

agent (10:1 ratio) were mixed in a disposable plastic dish and stirred for 5 minutes. The

mixture was degassed in a vacuum chamber at 12 psi for 20 minutes. Remaining bubbles

in the PDMS liquid were pipetted out.

The top layer mold was carefully filled with PDMS to avoid creating bubbles.

Manipulator clamps and hypodermic needles (25G) were used to hold the SMA wire

(050HT, Flexinol, Irvine, CA) (Fig. 5.3). Both ends of an 8cm long (for easier handling), 50

μm diameter SMA wire were inserted through the needle to create a small wire loop at

the needle tip. The filled mold and the manipulator clamps holding the two SMA wire

loops were placed onto a hotplate, and the SMA wire loops were submerged in fluid

PDMS at the plunger locations, taking care to avoid touching the needle tip to the PDMS.

The mold filled with PDMS was baked at 90℃ for 30 minutes. The cured PDMS was then

carefully peeled off.
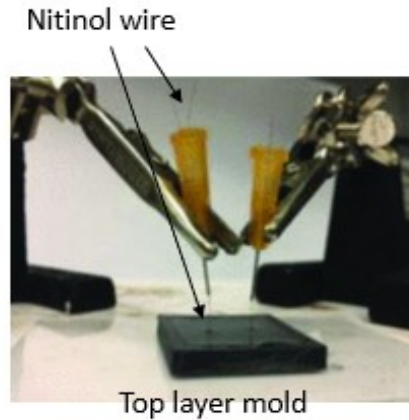
Figure 43.3 The embedding of Nitinol wire into the top PDMS layer.

The mold is filled with uncured PDMS mixture and is placed on a hotplate for PDMS curing.

PDMS was poured over the middle layer mold and cured on a hotplate at 90℃ for 30 minutes. The cured PDMS was then carefully peeled off.

The bottom PDMS layer is a four-chamber structure with the current delivery electrode positioned in each chamber (Fig. 5.4). We choose PEDOT:PSS electrodes due to its high CIC. [29] The electrode was designed to safely transfer 3mC charge (e.g., 1mA DC for 3 seconds or 3mA DC for 1 second) without causing irreversible electrochemical
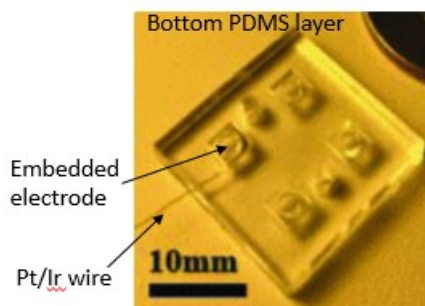
Figure 44.4 The bottom PDMS layer with four electrode chambers.

A current delivery electrode is embedded in one of the chambers and is connected with a Pt/Ir wire lead used for the connection with the external electronic board.

reactions in the electrolyte. Each electrode is constructed with four stacked 5mm*5mm carbon cloth pieces to meet the required surface area estimated with a CIC value of 3.6mC for PEDOT:PSS electrode. A 10 cm length of 0.15mm diameter Pt/Ir wire was connected to each electrode stack. The Pt/Ir wire lead can be used to connect with external electrical device and circuit. We coated the carbon cloth stack with PEDOT:PSS suspension liquid (3 wt%) then dried the electrodes in open air for 24 hours. Since two of the electrodes serve as cathodes and the other two electrodes serve as anodes in the first current phase then swap their polarities periodically to deliver charge-balanced current waveform, the electrodes need to be treated differently according to their first electrode polarities to maximize their CICs. The electrodes that serve as the cathodes in the first current phase will receive electrons from the connected circuit thus, need to be fully oxidized (i.e., $PEDOT^+A^-$ formation) by applying current flowing toward the treated electrodes. The electrodes that serve as the anodes in the first current phase will donate electrons to the circuit thus, need to be fully reduced (i.e., $PEDOT^0$ formation) by applying current flowing away from the treated electrodes. The rate of the electrochemical process of this electrode treatment was limited by setting the applied treatment current as 10μA to avoid high voltage that would induce delamination of the coating layer and uneven treatment on the electrode surface. The required duration of the treatment was roughly estimated by using a CIC value of 3.6mC per cm^2 and the surface area of $1cm^2$ for each electrode. The completion of the treatment of the electrode can be visually observed by adding a pH-sensitive dye in the electrolyte surrounding the treated electrodes. Once the

electrode is fully oxidized or reduced, further charge transfer of the current applied in the same direction would cause pH change in the electrolyte which could be seen by the color of the pH dye. The prepared electrode is embedded in the electrode chamber with the Pt/Ir wire lead penetrating through the PDMS used to connect with the electronic board controlling the current delivery through the electrode.

Corona discharge (BD-20AC, Electro-Technic products, Chicago, IL) was used to treat bonding surfaces of the PDMS pieces. The three PDMS layers were bonded sequentially from top to bottom to create the top and bottom channel networks in figure 5.5 (the
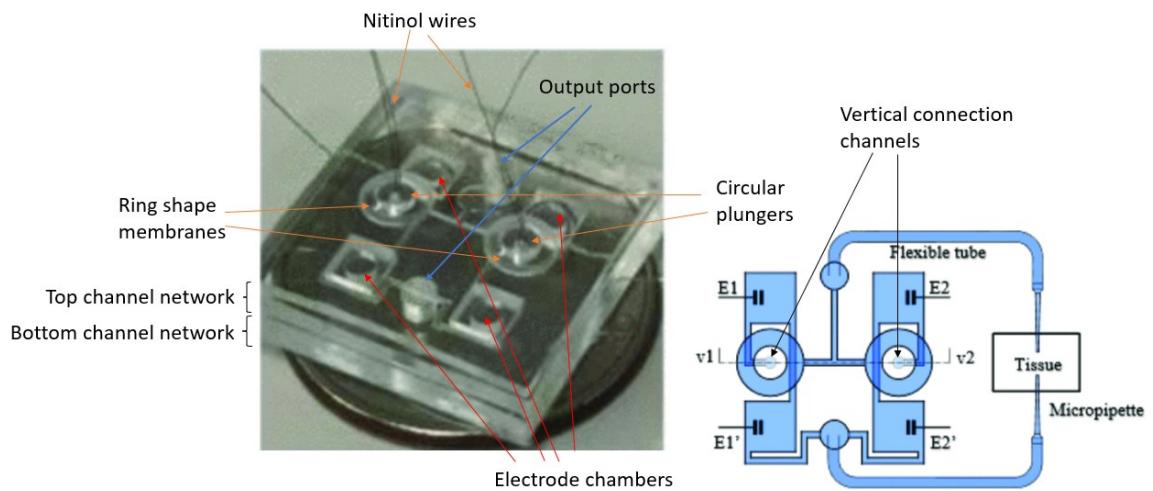
Figure 45.5 Bonded three-layer PDMS chip.

The left is a picture of the µF chip. The top channel network of this µF chip contains two Nitinol wire microvalves constructed with the circular plunger and the ring shape membrane. The bottom channel network contains four electrodes embedded in the chambers and two output ports used to deliver ionic DC to the tissue. The right is the diagram of the chip structure filled with electrolyte (blue). Two vertical channels that connect the top and bottom µF networks are controlled by the circular plungers of the valves (v1 and v2). The tubing connects the output ports with the target tissue.

picture on the left). Each surface treatment took 30-40 seconds. The corona discharge

head was as close to the surface as possible to maximize the bonding strength. However,

the embedded metal components (SMA wires and Pt electrodes) will induce breakdown

and burning short if the head is too close. To avoid breakdown, we increased the

treatment distance on the electrode area and increased the treatment time to achieve

equivalent bonding strength. The diagram of the chip structure is shown in Fig. 5.5 (on

the right).

To complete the structure of the microvalves, a 2mm thick black spacer printed by

the 3D printer was glued to the PDMS chip with a commercial fast-acting adhesive (all-

purpose glue, Krazy Glue, High Point, NC) to create space between the PCB layer and top

PDMS layer for plungers to be pulled. A 20×20mm^2 PCB (Radioshack, Fort Worth, TX) was

then glued on the spacer (Fig. 5.6). A slot in the center of PCB board was cut to allow SMA
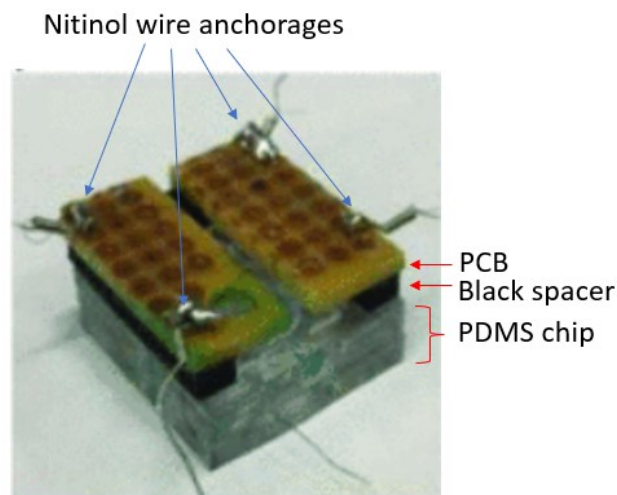
Figure 46.6 The anchorage of the nitinol wire.

A black spacer is added between the PCB and the PDMS chip. The nitinol wires are anchored on
the PCB.

wires to be fed through. As it is difficult to solder SMA wire directly, we sheathed the SMA

wire with a miniature slug of copper wire and squeezed the joint tightly to form a secured

mechanical and electrical connection. The SMA wire length between the two metal joints

was around 20mm to fit the chip size for both wires, the loose ends of the wires were

trimmed off. The copper joints were then soldered onto the PCB. The soldering/anchoring

positions on the PCB affect the tension of the wire. Overly tight wire pulls on the plunger,

causing the resting valve to open. Loose wire prevents the actuated wire from applying

pull force. We soldered the joints after taking the slack out of the SMA wires, but without

introducing leaks of the valves.

To measure the ionic current at the output, an ionic current sensor is embedded in

the return tubing shown in figure 5.7. The impedance of the channel between the S1 and
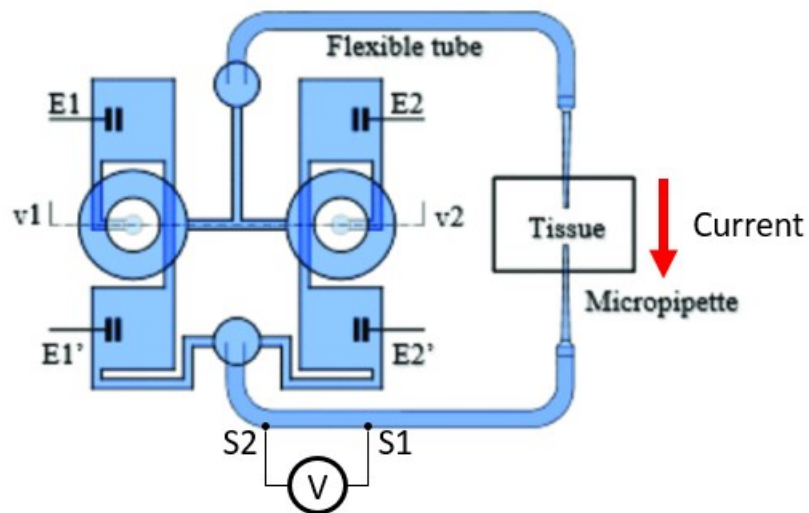
Figure 47.7 The ionic current sensor.

The Pt/Ir electrodes (S1 and S2) of the ionic current sensor are embedded in the tubing that

connects with the tissue. The ionic current flows out of the chip from the top output port and

returns to the chip via the bottom output port. The sensor is in the return tubing.

S2 Pt/Ir electrodes needs to be at least 10KΩ to make the sensor generate a 10mV change of the sensed voltage signal when the current changes by 1uA (a reasonable resolution for the output current of FS). As we characterized in chapter 4, the random noise of the sensed voltage signal of the sensor using Pt/Ir electrodes is ±2.1mV. Thus, the signal-to-noise ratio (SNR) is ~5 when the channel impedance between S1 and S2 is 10KΩ.

5.2 The Control cycle

To avoid the current interruption at the output of the FS caused by valve switching delays, we increased the duty cycle of the 105mA driving currents for the valves from 50% (figure 5.8a) to 68% (figure 5.8b) such that, as we hypothesized, the valves will be activated to open 0.4s earlier to eliminate the possibility of both valves being closed.

Based on the driving currents of the valves, we redesigned the control of the current delivery via the PEDOT:PSS electrodes embedded in the μF chip. The current delivery must
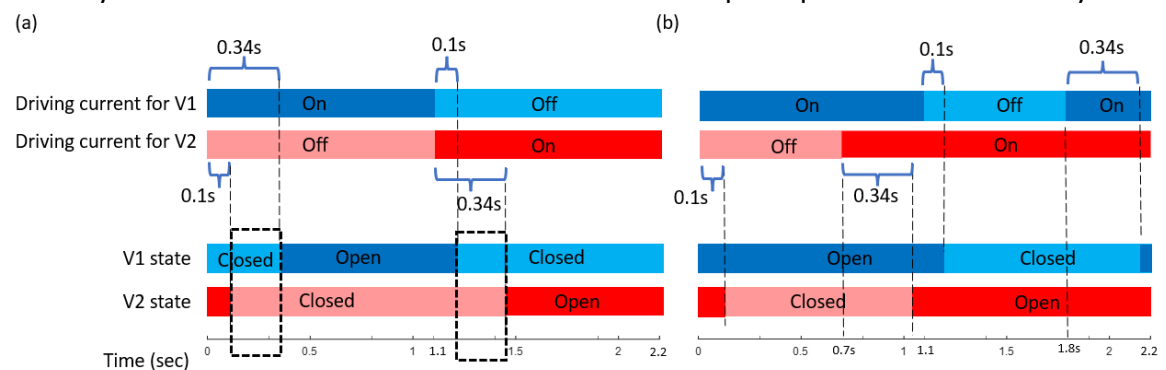
Figure 48.8 The estimated valves' states when operated with 50% and 68% duty cycle. The 105mA driving currents for the V1 and V2 in one operational cycle are shown on the top bars with the closed-to-open (0.34s) and open-to-closed (0.1s) switching delays. The corresponding valves' states are shown at the bottom bars. The durations when both valves are closed are labeled with squares with black dashed lines. (a) The valves are driven with 50% duty cycle. (b) The valves are driven with 68% duty cycle that opens the valves earlier.

complete two tasks to fulfill the working principle of the FS. The first task is to maintain

the constant DC at the output. This requires at least one pair of the electrodes (E1 and E1'

or E2 and E2') to be able to deliver current to the tissue throughout the cycle. The

corresponding valve must be open. The second task is to discharge when the electrode

pair is off the duty to maintain the DC output and the corresponding valve is closed. By

implementing these rules, we designed the current delivery in the μF chip as is shown in

figure 5.9. To minimize the fluctuation of the DC output caused by the changing
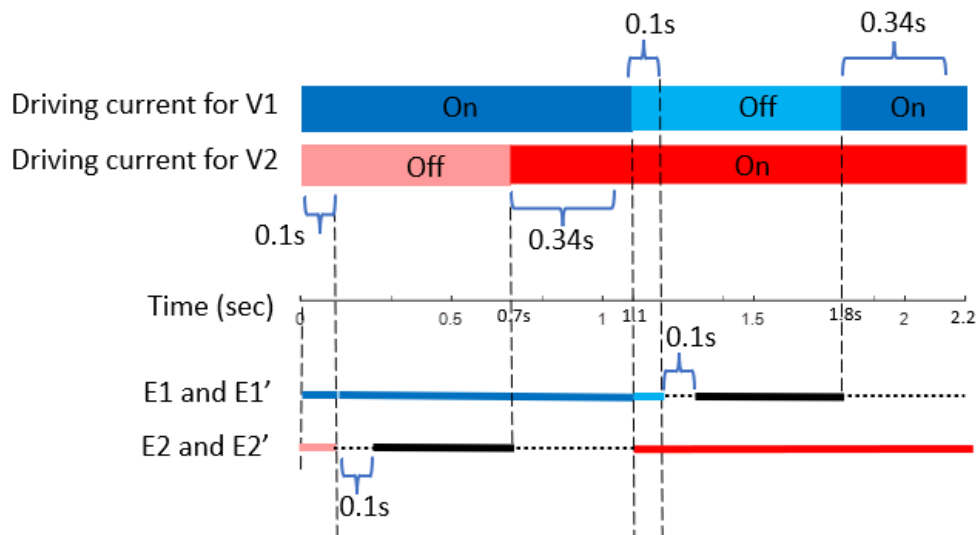
Figure 49.9 The current delivery via each electrode pair.

The bottom lines indicate the current delivery via each electrode pair. For the E1 and E1' electrode

pair, the dark blue line is the duration when the E1 electrode pair is on duty to maintain the

output. The light blue line is the duration when the current via the E1 electrode pair decreases

over time to zero. For the E2 and E2' electrode pair, the red line is the duration when the E2

electrode pair is on duty to maintain the output. The pink line is the duration when the current

via the E2 electrode pair decreases over time to zero. The black lines are the durations when the

electrode pairs discharge. And the black dashed lines are the durations when the current via the

electrode pair is zero.

impedance of the valves during their switching, the electrode pair on duty will adjust its current delivery based on the error between the commanded and actual outputs of the FS. As the delivered current can partially route via the discharging channels, the gain of this proportional controller is increased to be 2 to achieve a fast correction to an error while prevent overcompensation. The role switching (on/off duty) of the electrode pairs needs to be accomplished without causing interruption at the DC output. During this process (the light blue and pink lines in figure 5.9), we switch one electrode pair off the duty and linearly ramp down its current delivery to zero while assign the other electrode pair the duty to maintain the DC output. For example (the light blue line), the E1 electrode pair will linearly decrease its current delivery to zero within 0.1s while the E2 electrode pair will increase its current delivery to maintain the DC output. Since the setting of the FS updates every millisecond, this gradual change of the current delivery is necessary to prevent the occurrence of a significant error at the output. The electrode pairs are allowed to discharge within the 0.5s windows (black lines). The amplitude of the discharging current is calculated with the accumulated charge injection at the electrodes such that the electrodes are charge balanced after discharging.

5.3 Results and discussions

To test the AC to DC rectification of the FS, we fabricated one μF chip and operated it with the designed control cycle. In this test, the two output ports of the μF chip were connected with a 12.8cm long catheter (1.6mm inner diameter) to complete its output route and to mimic the output impedance (~50kΩ) of the FS comprising the impedances

of the output leads and the target tissue. (Figure 5.10) The µF chip and catheter were filled with 0.9% saline. The impedance of the discharging channel was 50KΩ with which we expected ~50% of the current delivered via the electrodes will be delivered to the output catheter when the valve is open (2kΩ impedance for an open valve). The Pt/Ir wire leads from the sensor and electrodes and the copper wire leads from the valves are soldered on a mounting board which is then connected with external electronic devices to operate the µF chip. During the test, we set the commanded output to be 50µA and measured the current delivery via each electrode pair and the DC output of the FS. Figure 5.11 shows the example waveforms of these measured parameters in one operational cycle. As shown in the blue waveform, the output of the FS measured by the ionic current
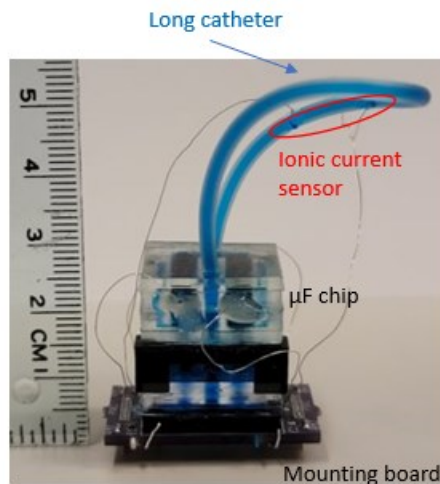
Figure 50.10 The picture of a fully assembled µF chip.

The picture of the µF chip on top of a mounting board used to connect with external electronic devices. The long catheter connects the two output ports of the µF chip. An ionic current sensor is embedded in the catheter. The µF chip and the long catheter are filled with 0.9% saline dyed blue.
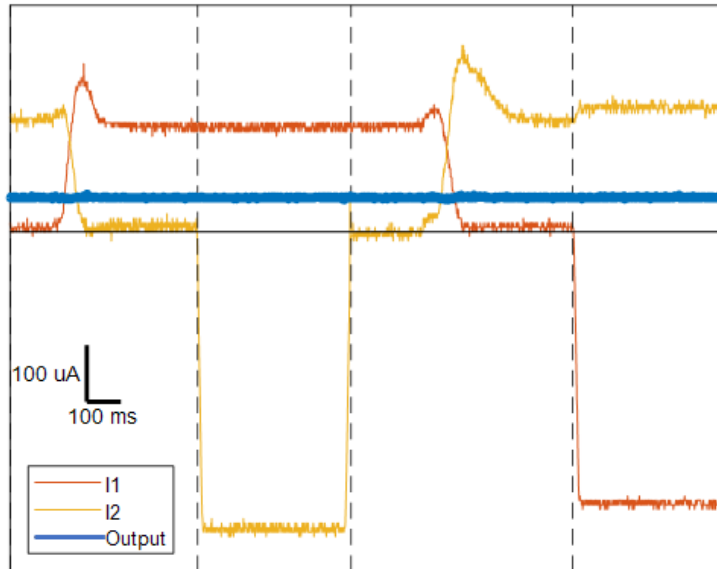
Figure 51.11 The test result of the AC to DC rectification of the FS.

This plot shows the measured parameters in one operational cycle. I1 (red line) is the current delivered via the E1 electrode pair. I2 (yellow) is the current delivered via the E2 electrode pair. The blue line is the measured output of the FS.

sensor remained at 50μA with a fluctuation range of ±5μA which is larger than the desired

1μA output resolution of the FS. This large fluctuation of the output current could be

caused by the unstable current delivery via the electrode pairs (I1 and I2) fluctuating with

a ±4μA range (red and yellow waveforms). The proportional control (P control only) of the

current delivery may lead the system to overly respond to a small error at the output (e.g.,

±2.1mV voltage noise between the two sensing electrodes of ionic current sensor) such

that I1 and I2 became unstable. The I1 and I2 waveforms are identical in shape but slightly

different in amplitude. This is because the open and closed impedances of the two

microvalves were slightly different due to the manual fabrication. Finally, we calculated

the charge injection at the electrodes with the obtained I1 and I2 waveforms in one

operational cycle. The net charge injection of each electrode pair was zero with negligible residue that may be caused by the measurement error of the electronic device.

To test if the FS could also be used to output other complex waveforms while maintain the charge balance at the electrodes, we commanded the output to be a sinusoidal current (0.55s period and 25μA amplitude) with an +25μA offset. Figure 5.12 shows the result of this test in one operational cycle. According to the measurement of the ionic current sensor, the FS output a sine current as we commanded but with an issue of a large fluctuation (±5μA) which was also observed in the previous AC to DC rectification. As calculated, in one operational cycle, the net charge injection of each electrode pair in this sine wave test was zero with negligible residue.
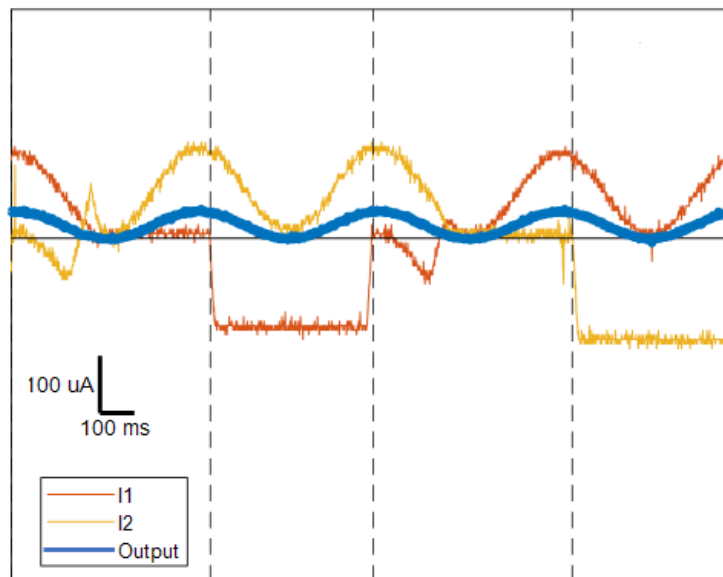
Figure 52.12 The test result of using the FS to output a sine current with an offset.
This plot shows the measured parameters in one operational cycle. I1 (red line) is the current delivered via the E1 electrode pair. I2 (yellow) is the current delivered via the E2 electrode pair. The blue line is the measured output of the FS.

Chapter 6

Conclusion

Electrical pulses can be applied to human body to treat many neural disorders which leads to the invention of the implantable pulse generator (IPG) that applies charge-balanced pulses to stimulate neurons. On the other hand, direct current (DC) that can suppress neural activity is prevented from being applied to human body for long durations due to the harmful electrolysis caused by the unbalanced charge injection at the electrodes. To overcome this barrier, inspired by electronic AC to DC bridge rectifier we invented a device called freeform stimulator (FS) (previously called safe direct current stimulator (SDCS)) that delivers charge-balanced currents into a µF chip via electrodes then, by controlling the current paths in the µF chip, rectifies the currents into a DC at the output. The µF chip requires two actuators to control the ionic paths in the chip, one ionic current sensor to measure the output and four embedded electrodes to deliver currents into the chip.

CHAPTER 6

In this thesis, we discussed the development of the required components in the μF chip of the FS. We developed a Nitinol wire actuated microvalve for a mechanical control of the ionic paths in the μF chip. This valve requires ~2V to operate and can be rapidly switched open/closed with 0.34s closed-to-open and 0.1s open-to-closed switching delays. This microvalve is suitable to be used to control the ionic paths in the FS due to its low operational voltage and rapid switching.

As eliminating the mechanical moving parts in the μF could improve the reliability of the FS, we developed an ionic transistor using ion exchange membranes, a non-mechanical actuator, that controls the impedance of a channel by depleting and enriching the ions in the channel. The current design of the transistor requires 40V to operate and takes 40s to switch on/off. To be used in the FS, the transistor needs an improvement in its performance which can be possibly achieved by miniaturizing the space between the membranes according to the simulation results. In the current fabrication of the transistor, the thinness of the space is limited by the thinness of the paper commercially available.

We also developed an ionic current sensor that uses two Pt/Ir electrodes to measure the voltage drop along a channel then calculates the ionic current passing through the channel by dividing the measured voltage drop with the impedance of the channel. This sensor can reliably measure ionic current with 1μA resolution and a ~5 SNR when the impedance of the channel between its two sensing electrodes is 10kΩ.

CHAPTER 6

Finally, we integrated all required μF components into one single chip to test the AC

to DC rectification of the FS. We commanded the output of the FS to be +50μA DC, and

the output was measured as +50μA DC with ±5μA fluctuation. We also commanded the

output to be a sinusoidal wave (0.55s period and 25μA amplitude) with an +25μA offset,

and the FS output a same sinusoidal waveform (with ±5μA fluctuation) as we

commanded. For all tested cases, the charge injection at each electrode pair was

commanded to be balanced (net zero charge injection) in each control cycle and was

verified by integrating the measured I1 and I2 over time.

To verify the elimination of irreversible electrolysis in the FS, the conducted FS test

uses the peak charge injection at the electrode in each cycle to compare with the

theoretical CIC of the electrode. To be more accurate, the fabricated electrodes that

deliver current into the μF chip need to be characterized with cyclic voltammetry to

obtain its realistic CIC. Additionally, a chemical essay that can detect irreversible

electrolysis at the electrodes can be implemented into the test of the FS to verify the

elimination of irreversible electrolysis during the operation of the FS.

Current lifetime of the μF chip is ~4 hours which was significantly impaired by the

evaporation of the water in the chip because the chip was exposed to the air during the

test. Possible improvement can be made by encapsulating the chip with materials (e.g.,

oil) that can isolate the chip from external air. This requires a design of an encasement

that can contain the μF chip within the isolating material.

References

[1]   C. Hammond, *Cellular and Molecular Neurophysiology: Fourth Edition*. 2015. doi:
        10.1016/C2011-0-07267-8.

[2]   M. J. A. M. van Putten, "Electrophysiology of the Neuron," in *Dynamics of Neural
        Networks*, 2020. doi: 10.1007/978-3-662-61184-5_1.

[3]   E. Paglia and J. Carter, "Cardiac Pacemakers," *Hospital Medicine Clinics*, vol. 6, no.
        3. 2017. doi: 10.1016/j.ehmc.2017.04.007.

[4]   J. G. Naples and M. J. Ruckenstein, "Cochlear Implant," *Otolaryngologic Clinics of
        North America*, vol. 53, no. 1. 2020. doi: 10.1016/j.otc.2019.09.004.

[5]   A. P. Fornos *et al.*, "The vestibular implant: A probe in orbit around the human
        balance system," *J. Vestib. Res. Equilib. Orientat.*, vol. 27, no. 1, 2017, doi:
        10.3233/VES-170604.

[6]   C. Günter, J. Delbeke, and M. Ortiz-Catalan, "Safety of long-term electrical
        peripheral nerve stimulation: Review of the state of the art," *Journal of
        NeuroEngineering and Rehabilitation*, vol. 16, no. 1. 2019. doi: 10.1186/s12984-
        018-0474-8.

REFERENCES

[7]   J. C. Gwilliam and K. Horch, "A charge-balanced pulse generator for nerve

        stimulation applications," *J. Neurosci. Methods*, vol. 168, no. 1, 2008, doi:

        10.1016/j.jneumeth.2007.09.004.

[8]   K. W. Horch and G. S. Dhillon, *Neuroprosthetics Theory and Practice*, vol. 53, no.

        9. 2004.

[9]   A. Groß and S. Sakong, "Modelling the electric double layer at

        electrode/electrolyte interfaces," *Current Opinion in Electrochemistry*, vol. 14.

        2019. doi: 10.1016/j.coelec.2018.09.005.

[10]   F. P. Aplin and G. Y. Fridman, "Implantable Direct Current Neural Modulation:

        Theory, Feasibility, and Efficacy," *Frontiers in Neuroscience*, vol. 13. p. 379, 2019.

        doi: 10.3389/fnins.2019.00379.

[11]   D. M. Ackermann, N. Bhadra, E. L. Foldes, K. L. Kilgore, and K. L. Kilgore,

        "Separated interface nerve electrode prevents direct current induced nerve

        damage.," *J. Neurosci. Methods*, vol. 201, no. 1, pp. 173–6, Sep. 2011, doi:

        10.1016/j.jneumeth.2011.01.016.

[12]   M. Manca, E. Glowatzki, D. C. Roberts, G. Y. Fridman, and F. P. Aplin, "Ionic direct

        current modulation evokes spike-rate adaptation in the vestibular periphery.,"

        Sci. Rep., vol. 9, no. 1, p. 18924, Dec. 2019, doi: 10.1038/s41598-019-55045-6.

[13]   F. P. Aplin, D. Singh, C. C. Della Santina, and G. Y. Fridman, "Ionic Direct Current

        Modulation for Combined Inhibition/Excitation of the Vestibular System," in *IEEE

        Transactions on Biomedical Engineering*, 2020, vol. 66, no. 3, pp. 775–783. doi:

REFERENCES

10.1109/TBME.2018.2856698.Ionic.

[14]   D. Liebetanz *et al.*, "Anticonvulsant effects of transcranial direct-current

stimulation (tDCS) in the rat cortical ramp model of focal epilepsy," *Epilepsia*, vol.

47, no. 7, 2006, doi: 10.1111/j.1528-1167.2006.00539.x.

[15]   D. San-Juan *et al.*, "Transcranial direct current stimulation in epilepsy," *Brain

Stimulation*, vol. 8, no. 3. 2015. doi: 10.1016/j.brs.2015.01.001.

[16]   A. J. Woods *et al.*, "A technical guide to tDCS, and related non-invasive brain

stimulation tools," *Clinical Neurophysiology*, vol. 127, no. 2. 2016. doi:

10.1016/j.clinph.2015.11.012.

[17]   F. Mina *et al.*, "Model-guided control of hippocampal discharges by local direct

current stimulation," *Sci. Rep.*, vol. 7, no. 1, 2017, doi: 10.1038/s41598-017-

01867-1.

[18]   F. Yang *et al.*, "Differential expression of voltage-gated sodium channels in

afferent neurons renders selective neural block by ionic direct current," *Sci. Adv.*,

vol. 4, no. 4, p. eaaq1438, Apr. 2018, doi: 10.1126/sciadv.aaq1438.

[19]   F. P. Aplin, D. Singh, C. C. Della Santina, and G. Y. Fridman, "Combined ionic direct

current and pulse frequency modulation improves the dynamic range of

vestibular canal stimulation," *J. Vestib. Res.*, pp. 1–8, 2019, doi: 10.3233/ves-

190651.

[20]   G. Y. Fridman and C. C. Della Santina, "Safe direct current stimulation to expand

capabilities of neural prostheses.," *IEEE Trans. Neural Syst. Rehabil. Eng.*, vol. 21,

REFERENCES

no. 2, pp. 319–28, Mar. 2013, doi: 10.1109/TNSRE.2013.2245423.

[21]   C. Cheng, F. P. Aplin, and G. Y. Fridman, "A microfluidic system integrated with shape memory alloy valves for a safe direct current delivery system," in *Proceedings of the Annual International Conference of the IEEE Engineering in Medicine and Biology Society, EMBS*, 2020, vol. 2020-July. doi: 10.1109/EMBC44109.2020.9176474.

[22]   G. Fridman, "Safe Direct Current Stimulator design for reduced power consumption and increased reliability," 2017. doi: 10.1109/EMBC.2017.8037015.

[23]   F. Blaabjerg, *Control of power electronic converters and systems*. 2018. doi: 10.1016/C2015-0-02427-3.

[24]   C. Cheng, R. Thakur, A. R. Nair, S. Sterrett, and G. Fridman, "Miniature Elastomeric Valve Design for Safe Direct Current Stimulator," *IEEE Biomed. Circuits Syst. Conf. Healthc. Technol. [proceedings]. IEEE Biomed. Circuits Syst. Conf.*, vol. 2017, pp. 1–4, Oct. 2017, doi: 10.1109/BIOCAS.2017.8325194.

[25]   C. Cheng, A. R. Nair, R. Thakur, and G. Fridman, "Normally closed plunger-membrane microvalve self-actuated electrically using a shape memory alloy wire," *Microfluid. Nanofluidics*, vol. 22, no. 3, pp. 1–9, 2018, doi: 10.1007/s10404-018-2049-1.

[26]   C. Cheng, G. Foxworthy, and G. Fridman, "On-chip ionic current sensor," *Appl. Phys. A Mater. Sci. Process.*, vol. 127, no. 5, 2021, doi: 10.1007/s00339-021-04469-x.

REFERENCES

[27]   J. Y. Qian, C. W. Hou, X. J. Li, and Z. J. Jin, "Actuation mechanism of microvalves: A review," *Micromachines*, vol. 11, no. 2. 2020. doi: 10.3390/mi11020172.

[28]   P. Gravesen, J. Branebjerg, and O. S. Jensen, "Microfluidics - A review," *Journal of Micromechanics and Microengineering*, vol. 3, no. 4. 1993. doi: 10.1088/0960-1317/3/4/002.

[29]   S. F. Cogan, "Neural stimulation and recording electrodes," *Annual Review of Biomedical Engineering*. 2008. doi: 10.1146/annurev.bioeng.10.061807.160518.

[30]   Y. Cong, S. Katipamula, T. Geng, S. A. Prost, K. Tang, and R. T. Kelly, "Electrokinetic sample preconcentration and hydrodynamic sample injection for microchip electrophoresis using a pneumatic microvalve," *Electrophoresis*, vol. 37, no. 3, 2016, doi: 10.1002/elps.201500286.

[31]   H. S. Chuang, R. Thakur, and S. T. Wereley, "Characterizations of gas purge valves for liquid alignment and gas removal in a microfluidic chip," *J. Micromechanics Microengineering*, vol. 22, no. 8, 2012, doi: 10.1088/0960-1317/22/8/085023.

[32]   A. M. Amin *et al.*, "Software-programmable continuous-flow multi-purpose lab-on-a-chip," *Microfluid. Nanofluidics*, vol. 15, no. 5, 2013, doi: 10.1007/s10404-013-1180-2.

[33]   J. Y. Back, J. Y. Park, J. Il Ju, T. S. Lee, and S. H. Lee, "A pneumatically controllable flexible and polymeric microfluidic valve fabricated via in situ development," *J. Micromechanics Microengineering*, vol. 15, no. 5, 2005, doi: 10.1088/0960-1317/15/5/017.

REFERENCES

[34] G. H. Feng and Y. C. Chou, "Fabrication and characterization of thermally driven fast turn-on microvalve with adjustable backpressure design," *Microelectron. Eng.*, vol. 88, no. 2, 2011, doi: 10.1016/j.mee.2010.10.011.

[35] S. Augustine, P. Gu, X. Zheng, T. Nishida, and Z. H. Fan, "Low-power electrically controlled thermoelastic microvalves integrated in thermoplastic microfluidic devices," *Microfluid. Nanofluidics*, vol. 19, no. 6, 2015, doi: 10.1007/s10404-015-1653-6.

[36] M. Díaz-González, C. Fernández-Sánchez, and A. Baldi, "Multiple actuation microvalves in wax microfluidics," *Lab Chip*, vol. 16, no. 20, 2016, doi: 10.1039/c6lc00800c.

[37] A. V. Desai, J. D. Tice, C. A. Apblett, and P. J. A. Kenis, "Design considerations for electrostatic microvalves with applications in poly(dimethylsiloxane)-based microfluidics," *Lab Chip*, vol. 12, no. 6, 2012, doi: 10.1039/c2lc21133e.

[38] A. T. Evans, J. M. Park, S. Chiravuri, and Y. B. Gianchandani, "A low power, microvalve regulated architecture for drug delivery systems," *Biomed. Microdevices*, vol. 12, no. 1, 2010, doi: 10.1007/s10544-009-9372-y.

[39] S. Chen *et al.*, "A normally-closed piezoelectric micro-valve with flexible stopper," *AIP Adv.*, vol. 6, no. 4, 2016, doi: 10.1063/1.4947301.

[40] E. Yildirim, M. A. S. Arikan, and H. Külah, "A normally closed electrostatic parylene microvalve for micro total analysis systems," *Sensors Actuators, A Phys.*, vol. 181, pp. 81–86, 2012, doi: 10.1016/j.sna.2012.05.008.

REFERENCES

[41]   Q. Zhang *et al.*, "On-demand control of microfluidic flow via capillary-tuned

solenoid microvalve suction," *Lab Chip*, vol. 14, no. 24, 2014, doi:

10.1039/c4lc00833b.

[42]   N. Li, C. Sip, and A. Folch, "Microfluidic chips controlled with elastomeric

microvalve arrays," *J. Vis. Exp.*, no. 8, 2007, doi: 10.3791/296.

[43]   X. Liu and S. Li, "An Electromagnetic Microvalve for Pneumatic Control of

Microfluidic Systems," *J. Lab. Autom.*, vol. 19, no. 5, 2014, doi:

10.1177/2211068214531760.

[44]   J. Mohd Jani, M. Leary, A. Subic, and M. A. Gibson, "A review of shape memory

alloy research, applications and opportunities," *Materials and Design*, vol. 56. pp.

1078–1113, 2014. doi: 10.1016/j.matdes.2013.11.084.

[45]   E. Henderson, D. H. Nash, and W. M. Dempster, "On the experimental testing of

fine Nitinol wires for medical devices," *J. Mech. Behav. Biomed. Mater.*, vol. 4, no.

3, 2011, doi: 10.1016/j.jmbbm.2010.10.004.

[46]   C. M. Pemble and B. C. Towe, "Miniature shape memory alloy pinch valve,"

Sensors Actuators, A Phys., vol. 77, no. 2, 1999, doi: 10.1016/S0924-

4247(99)00157-0.

[47]   S. Vyawahare, S. Sitaula, S. Martin, D. Adalian, and A. Scherer, "Electronic control

of elastomeric microfluidic circuits with shape memory actuators," *Lab Chip*, vol.

8, no. 9, 2008, doi: 10.1039/b804515a.

[48]   M. Kohl, D. Dittmann, E. Quandt, and B. Winzek, "Thin film shape memory

microvalves with adjustable operation temperature," *Sensors Actuators, A Phys.*, vol. 83, no. 1, 2000, doi: 10.1016/S0924-4247(99)00386-6.

[49] G. Sun, S. Senapati, and H.-C. Chang, "High-flux ionic diodes, ionic transistors and ionic amplifiers based on external ion concentration polarization by an ion exchange membrane: a new scalable ionic circuit platform," *Lab Chip*, vol. 16, no. 7, pp. 1171–1177, 2014, doi: 10.1039/c6lc00026f.

[50] Y. Lin, X. Liu, and T. Arai, "Capillary Ionic Transistor and Precise Transport Control for Nano Manipulation," in *International Conference on Robotics and Automation (ICRA)*, 2019, pp. 237–242.

[51] K. Tybrandt, E. O. Gabrielsson, and M. Berggren, "Toward Complementary Ionic Circuits: The npn Ion Bipolar Junction Transistor," *J. Am. Chem. Soc*, vol. 133, no. 26, pp. 10141–10145, 2011, doi: 10.1021/ja200492c.

[52] K. Tybrandt, K. C. Larsson, A. Richter-Dahlfors, and M. Berggren, "Ion bipolar junction transistors," *Proc. Natl. Acad. Sci. U. S. A.*, vol. 107, no. 22, pp. 9929–9932, Jun. 2010, doi: 10.1073/PNAS.0913911107/-/DCSUPPLEMENTAL/PNAS.0913911107_SI.PDF.

[53] Z. Jiang and D. Stein, "Charge regulation in nanopore ionic field-effect transistors," *Phys. Rev. E*, vol. 83, no. 3, 2011, doi: 10.1103/PhysRevE.83.031203.

[54] W. Guan, R. Fan, and M. A. Reed, "Field-effect reconfigurable nanofluidic ionic diodes," *Nat. Commun.*, vol. 2, no. 1, 2011, doi: 10.1038/ncomms1514.

[55] R. Karnik, R. Fan, M. Yue, D. Li, P. Yang, and A. Majumdar, "Electrostatic control of

REFERENCES

ions and molecules in nanofluidic transistors," *Nano Lett.*, vol. 5, no. 5, 2005, doi: 10.1021/nl050493b.

[56] K. Bohinc, V. Kralj-Iglič, and A. Iglič, "Thickness of electrical double layer. Effect of ion size," *Electrochim. Acta*, vol. 46, no. 19, 2001, doi: 10.1016/S0013-4686(01)00525-4.

[57] N. Liu, R. Chen, and Q. Wan, "Recent advances in electric-double-layer transistors for bio-chemical sensing applications," *Sensors (Switzerland)*, vol. 19, no. 15. 2019. doi: 10.3390/s19153425.

[58] E. O. Gabrielsson, K. Tybrandt, and M. Berggren, "Polyphosphonium-based ion bipolar junction transistors," *Biomicrofluidics*, vol. 8, no. 6, 2014, doi: 10.1063/1.4902909.

[59] S. Mafé and P. Ramfaz, "Electrochemical characterization of polymer ion-exchange bipolar membranes," *Acta Polym.*, vol. 48, no. 7, pp. 234–250, 1997, doi: 10.1002/actp.1997.010480702.

[60] H. D. Hurwitz and R. Dibiani, "Experimental and theoretical investigations of steady and transient states in systems of ion exchange bipolar membranes," *J. Memb. Sci.*, vol. 228, no. 1, pp. 17–43, 2004, doi: 10.1016/j.memsci.2003.09.009.

[61] M. R. Hamblin and M. Karimi, *Biomedical Applications of Microfluidic Devices*. 2021. doi: 10.1016/c2018-0-04779-9.

[62] T. Luo, S. Abdu, and M. Wessling, "Selectivity of ion exchange membranes: A review," *Journal of Membrane Science*, vol. 555. 2018. doi:

REFERENCES

10.1016/j.memsci.2018.03.051.

[63]   S. Abu Khalla and M. E. Suss, "Desalination via chemical energy: An electrodialysis
       cell driven by spontaneous electrode reactions," *Desalination*, vol. 467, pp. 257–
       262, 2019, doi: 10.1016/j.desal.2019.04.031.

[64]   G. Doornbusch, M. van der Wal, M. Tedesco, J. Post, K. Nijmeijer, and Z.
       Borneman, "Multistage electrodialysis for desalination of natural seawater,"
       Desalination, vol. 505, 2021, doi: 10.1016/j.desal.2021.114973.

[65]   M. Tedesco, H. V. M. Hamelers, and P. M. Biesheuvel, "Nernst-Planck transport
       theory for (reverse) electrodialysis: I. Effect of co-ion transport through the
       membranes," *J. Memb. Sci.*, vol. 510, pp. 370–381, 2016, doi:
       10.1016/j.memsci.2016.03.012.

[66]   M. La Cerva *et al.*, "Determination of limiting current density and current
       efficiency in electrodialysis units," *Desalination*, vol. 445, pp. 138–148, 2018, doi:
       10.1016/j.desal.2018.07.028.

[67]   I. Atlas, J. Wu, A. N. Shocron, and M. E. Suss, "Spatial variations of pH in
       electrodialysis stacks: Theory," *Electrochim. Acta*, vol. 413, pp. 140–151, 2022,
       doi: 10.1016/j.electacta.2022.140151.

[68]   A. H. Galama *et al.*, "Membrane resistance: The effect of salinity gradients over a
       cation exchange membrane," *J. Memb. Sci.*, vol. 467, pp. 279–291, 2014, doi:
       10.1016/j.memsci.2014.05.046.

[69]   A. H. Galama, N. A. Hoog, and D. R. Yntema, "Method for determining ion

exchange membrane resistance for electrodialysis systems," *Desalination*, vol. 380, pp. 1–11, 2016, doi: 10.1016/j.desal.2015.11.018.

[70] H. Strathmann, "Electrodialysis, a mature technology with a multitude of new applications," *Desalination*, vol. 264, no. 3, 2010, doi: 10.1016/j.desal.2010.04.069.

[71] E. O. Gabrielsson, P. Janson, K. Tybrandt, D. T. Simon, and M. Berggren, "A four-diode full-wave ionic current rectifier based on bipolar membranes: Overcoming the limit of electrode capacity," *Adv. Mater.*, vol. 26, no. 30, pp. 5143–5147, 2014, doi: 10.1002/adma.201401258.

[72] J. Isaksson, P. Kjäll, D. Nilsson, N. Robinson, M. Berggren, and A. Richter-Dahlfors, "Electronic control of Ca2+ signalling in neuronal cells using an organic electronic ion pump," *Nat. Mater.*, 2007, doi: 10.1038/nmat1963.

[73] D. T. Simon *et al.*, "Organic electronics for precise delivery of neurotransmitters to modulate mammalian sensory function," *Nat. Mater.*, 2009, doi: 10.1038/nmat2494.

[74] B. J. Baker *et al.*, "Imaging brain activity with voltage- and calcium-sensitive dyes," *Cell. Mol. Neurobiol.*, vol. 25, no. 2, 2005, doi: 10.1007/s10571-005-3059-6.

[75] K. D. Piatkevich *et al.*, "A robotic multidimensional directed evolution approach applied to fluorescent voltage reporters article," *Nat. Chem. Biol.*, vol. 14, no. 4, pp. 352–360, 2018, doi: 10.1038/s41589-018-0004-9.

[76] Y. Bar-Cohen and Q. Zhang, "Electroactive Polymer Actuators and Sensors," *MRS*

REFERENCES

Bull., 2008, doi: 10.1557/mrs2008.42.

[77] Y. Bar-Cohen, K. J. Kim, H. R. Choi, and J. D. W. Madden, "Electroactive polymer materials," *Smart Materials and Structures*, vol. 16, no. 2. 2007. doi: 10.1088/0964-1726/16/2/E01.

[78] V. L. D. S. N. Button, *Principles of Measurement and Transduction of Biomedical Variables*. 2015. doi: 10.1016/C2013-0-14261-4.

[79] F. L. H. Gielen and P. Bergveld, "Comparison of electrode impedances of Pt, PtIr (10% Ir) and Ir-AIROF electrodes used in electrophysiological experiments," *Med. Biol. Eng. Comput.*, 1982, doi: 10.1007/BF02441854.

[80] I. B. Obot, I. B. Onyeachu, A. Zeino, and S. A. Umoren, "Electrochemical noise (EN) technique: review of recent practical applications to corrosion electrochemistry research," *Journal of Adhesion Science and Technology*. 2019. doi: 10.1080/01694243.2019.1587224.

[81] A. Yúfera and A. Rueda, "A method for bioimpedance measure with four- and two-electrode sensor systems," 2008. doi: 10.1109/iembs.2008.4649662.